

FOREVER22: galaxy formation in protocluster regions

Hidenobu Yajima^{1*}, Makito Abe¹, Sadegh Khochfar², Kentaro Nagamine^{3,4,5},
 Akio K. Inoue⁶, Tadayuki Kodama⁷, Shohei Arata³, Claudio Dalla-Vecchia⁸,
 Hajime Fukushima¹, Takuya Hashimoto⁹, Nobunari Kashikawa¹⁰,
 Mariko Kubo¹¹, Yuexing Li¹², Yuichi Matsuda^{13,14}, Ken Mawatari¹⁵,
 Masami Ouchi^{4,13,15}, Hideki Umehata^{16,17}

¹Center for Computational Sciences, University of Tsukuba, Ten-nodai, 1-1-1 Tsukuba, Ibaraki 305-8577, Japan

²Institute for Astronomy, University of Edinburgh, Royal Observatory, Edinburgh, EH9 3HJ, UK

³Department of Earth and Space Science, Graduate School of Science, Osaka University, Toyonaka, Osaka 560-0043, Japan

⁴Kaoli IPMU (WPI), The University of Tokyo, 5-1-5 Kashiwanoha, Kashiwa, Chiba, 277-8583, Japan

⁵Department of Physics & Astronomy, University of Nevada, Las Vegas, 4505 S. Maryland Pkwy, Las Vegas, NV 89154-4002, USA

⁶Waseda Research Institute for Science and Engineering, Faculty of Science and Engineering, Waseda University, 3-4-1, Okubo, Shinjuku, Tokyo 169-8555, Japan

⁷Astronomical Institute, Tohoku University, Sendai 980-8578, Japan

⁸Instituto de Astrofísica de Canarias, C/Vía Láctea s/n, 38205 La Laguna, Tenerife, Spain

⁹Tomonaga Center for the History of the Universe (TCHO), Faculty of Pure and Applied Sciences, University of Tsukuba, Tsukuba, Ibaraki 305-8571, Japan

¹⁰Department of Astronomy, Graduate School of Science, The University of Tokyo, 7-3-1 Hongo, Bunkyo, Tokyo 113-0033, Japan

¹¹Research Center for Space and Cosmic Evolution, Ehime University, Matsuyama, Ehime 790-8577, Japan

¹²Department of Astronomy and Astrophysics, The Pennsylvania State University, University Park, PA 16802, USA

¹³National Astronomical Observatory of Japan, 2-21-1 Osawa, Mitaka, Tokyo 181-8588, Japan

¹⁴Department of Astronomical Science, SOKENDAI (Graduate University for Advanced Studies), Osawa 2-21-1, Mitaka, Tokyo 181-8588, Japan

¹⁵Institute for Cosmic Ray Research, The University of Tokyo, 5-1-5 Kashiwa-no-Ha, Kashiwa, Chiba 277-8582, Japan

¹⁶RIKEN Cluster for Pioneering Research, 2-1 Hirosawa, Wako-shi, Saitama 351-0198, Japan

¹⁷Institute of Astronomy, School of Science, The University of Tokyo, 2-21-1 Osawa, Mitaka, Tokyo 181-0015, Japan

Accepted ?; Received ??; in original form ???

ABSTRACT

We present results from a new cosmological hydrodynamics simulation campaign of protocluster (PC) regions, FOREVER22: FORMation and EVolution of galaxies in Extremely-overdense Regions motivated by SSA22. The simulations cover a wide range of cosmological scales using three different zoom set-ups in a parent volume of (714.2 Mpc)³: PCR (Proto-Cluster Region; $V = (28.6 \text{ Mpc})^3$ and SPH particle mass, $m_{\text{SPH}} = 4.1 \times 10^6 M_{\odot}$), BCG (Brightest proto-Cluster Galaxy; $V \sim (3 \text{ Mpc})^3$ and $m_{\text{SPH}} = 5.0 \times 10^5 M_{\odot}$), and First ($V \sim (0.4 \text{ Mpc})^3$ and $m_{\text{SPH}} = 7.9 \times 10^3 M_{\odot}$) runs, that allow to focus on different aspects of galaxy formation. In the PCR runs, we follow 10 PCs, each harbouring 1 - 4 SMBHs with $M_{\text{BH}} \geq 10^9 M_{\odot}$. One of the PC cores shows a spatially close arrangement of seven starburst galaxies with $\text{SFR} \gtrsim 100 M_{\odot} \text{ yr}^{-1}$ each, that are dust-obscured and would appear as submillimeter galaxies with flux $\gtrsim 1 \text{ mJy}$ at 1.1 mm in observations. The BCG runs show that the total SFRs of haloes hosting BCGs are affected by AGN feedback, but exceed $1000 M_{\odot} \text{ yr}^{-1}$ at $z \lesssim 6$. The First runs resolve mini-haloes hosting population (Pop) III stars and we show that, in PC regions, the dominant stellar population changes from Pop III to Pop II at $z \gtrsim 20$, and the first galaxies with $\text{SFR} \gtrsim 18 M_{\odot} \text{ yr}^{-1}$ form at $z \sim 10$. These can be prime targets for future observations with the *James Webb Space Telescope*. Our simulations successfully reproduce the global star formation activities in observed PCs and suggest that PCs can kickstart cosmic reionization.

Key words: radiative transfer – stars: Population III – galaxies: evolution – galaxies: formation – galaxies: high-redshift

1 INTRODUCTION

Understanding galaxy evolution in the early Universe is one of the major goals in astrophysics. The recent development of observational facilities has allowed us to probe high-redshift galaxies and the large-scale structure of the Universe. Observations with optical/near-infrared telescopes have successfully observed numerous high-redshift galaxies with the drop-out technique, called “Lyman-break galaxies (LBGs)” (e.g., Shapley 2011; Bouwens et al. 2015; Oesch et al. 2016; Ouchi et al. 2018). Also, some of them have been detected with strong Ly α or H α lines originated from ionized gas due to young stars, called “Lyman-alpha emitters (LAEs)” and “H α emitters (HAEs)” (e.g., Iye et al. 2006; Finkelstein et al. 2013; Ono et al. 2018; Hayashi et al. 2020). This progress has led to a consensus on the evolution of the cosmic star formation rate densities (CSFRDs) between $z = 0$ and $z \sim 10$ (e.g., Madau & Dickinson 2014; Bouwens et al. 2015, 2020). In addition to the detections of direct stellar radiation, recent observations using submillimeter telescopes, e.g., the Atacama Large Millimeter/submillimeter Array (ALMA) have detected dust thermal emission from distant galaxies, called “submillimeter galaxies (SMGs)” (e.g., Chapman et al. 2005; Riechers et al. 2013; Hatsukade et al. 2018; Marrone et al. 2018). As the galaxy mass increases, star-forming regions can be enshrouded by dust because of higher metallicity and dust content (Casey et al. 2014). Therefore the submillimeter flux can be a powerful tool to probe massive galaxies with active star formation. Moreover, [OIII] 88 μm or [CII] 158 μm lines from distant galaxies have been successfully detected with ALMA (Capak et al. 2015; Inoue et al. 2016). E.g. Hashimoto et al. (2018) have spectroscopically confirmed the most distant galaxies at $z = 9.1$ via the detection of the [OIII] 88 μm line (see also the most distant galaxy without line detection at $z = 11.1$: Oesch et al. 2016). While it seems evident that the various observational properties are likely linked with fundamental physical properties such as star formation, distribution of gas and dust and gas kinematics, the exact connection is still poorly understood.

According to the current standard paradigm of structure formation, galaxies evolve via mergers and matter accretion from large-scale filaments (e.g., Springel et al. 2006). The growth rates of galaxies sensitively depend on formation sites. In overdense regions, galaxies rapidly grow, while galaxies in void regions do slowly (e.g., Benson et al. 2003). Therefore, understanding the environmental effects can be a key to reveal various evolutionary scenarios for high-redshift galaxies. In overdense regions, galaxies cluster on shorter length scales (see the review by Overzier 2016). Theoretical models based on cosmological N -body simulations indicated that regions with a higher level of clustering at early times will evolve into present-day galaxy clusters at $z \sim 0$ (Chiang et al. 2017). It therefore makes sense to associate such regions as “protoclusters (PCs)” regions, a term we will use throughout this paper. As a typical protocluster in the early Universe, the region SSA22 at $z = 3.1$ has been investigated by various observational techniques. E.g. the large scale filamentary structure around SSA22 has been studied using the spatial distributions of LAEs (Hayashino et al. 2004; Matsuda et al. 2004). Giant Lyman-alpha blobs (LABs) with sizes of $\gtrsim 100$ kpc have been reported at the core of SSA22

(Steidel et al. 2000; Matsuda et al. 2012). Tamura et al. (2009) showed that SMGs distributed near LAEs in SSA22 (see also, Umehata et al. 2015, 2018, 2019). These observations suggest that various galaxies can form and coexist in such an overdense regions. Therefore, PCs have the potential to be laboratories to understand the diversity of galaxy evolution.

A recent wide survey with Subaru Hyper Supreme Cam observed $\gtrsim 200$ candidates of protoclusters composed of LBGs at $z \gtrsim 4$ (Toshikawa et al. 2018). Harikane et al. (2019) discovered a protocluster with LAEs/LABs at $z > 6$ (see also, Ishigaki et al. 2016). Also, Miller et al. (2018) discovered a clustered region of dusty starburst galaxies at $z = 4$ where the total star formation rate of observed galaxies at the PC core exceeded $6000 M_{\odot} \text{ yr}^{-1}$ (see also, Oteo et al. 2018). Thus, recent observations have allowed us to study galaxy formation in PCs, and as such the onset of environmental effects.

Combining cosmological N -body simulations and semi-analytical galaxy formation models, Chiang et al. (2017) investigated star formation in PCs. They suggested that PCs contributed significantly to the cosmic star formation rate density (CSFRD) at high-redshift $z \gtrsim 2$ and trigger cosmic reionization. Recent hydrodynamics simulations of galaxy formation in large-scale structures have studied star formation, gas dynamics, and stellar/AGN feedback processes (e.g., Vogelsberger et al. 2014). Using the moving mesh hydrodynamics code AREPO (Springel 2010), the Illustris/illustris-TNG projects showed results for cosmological hydrodynamics simulations of cosmic volumes of $(50 - 100 \text{ cMpc})^3$, and successfully reproduced various properties of the local galaxies population (e.g., Nelson et al. 2018; Pillepich et al. 2018b). In a similar project (EAGLE project) using a smoothed particle hydrodynamics (SPH) code Schaye et al. (2015, hereafter S15) reproduced physical properties of the local galaxy population. They introduced sub-grid models associated with star formation and black holes and their feedback processes with tuned parameters (see also, Crain et al. 2015). As indicated by the comparison between stellar and halo mass functions, stellar feedback can regulate star formation in low-mass galaxies and the feedback from active galactic nuclei (AGNs) regulates star formation in massive galaxies. The above projects applied feedback models to successfully regulate the star formation activities of low-mass and massive galaxies appropriately. Dubois et al. (2016) studied the impacts of AGNs on galaxies and the circum-galactic medium (CGM) in the HORIZON-AGN simulation with the adaptive mesh refinement code, RAMSES (Teyssier 2002). They indicated that the morphology of massive galaxies sensitively depended on AGN feedback (see also, Sijacki et al. 2015; Di Matteo et al. 2017; Tremmel et al. 2017). Thus, the recent developments of simulation codes and sub-grid models have allowed us to model galaxies reproducing statistical properties of local galaxies as inferred from an average over different environments and study physical processes to determine star formation and BH activities and the distribution of gas and stars.

On the other hand, galaxy evolution in overdense regions has not been studied and understood well. Barnes et al. (2017) consider a huge cosmological volume of $(3.2 \text{ Gpc})^3$ and selected 30 galaxy clusters at $z = 0$. They studied the 30 clusters with zoom-in simulations with the calculation code

developed in EAGLE project, which is called the Cluster-Eagle project. Their simulations reproduced stellar and BH components in local galaxy clusters, while the gas fraction was too high. Also, Cui et al. (2018) investigated statistical properties of galaxy clusters for a sample of 324 clusters (The Three Hundred project) based on zoom-in simulations with a modified version of SPH code, GADGET2 (Springel 2005). They showed the baryonic fraction of the clusters matched observations, while there were some differences in the masses of member galaxies and their colors. Thus, while recent simulations successfully reproduced observed properties of local galaxy clusters partially, baryonic physics in the overdense regions is still puzzling. Recently, Trebitsch et al. (2020) studied a protocluster, the most massive halo in a volume of $(100 \text{ cMpc})^3$, and investigated the contribution to cosmic reionization in their simulation, the OBELISK, which is the updated version of the HORIZON-AGN project. They investigated the onset of cosmic reionization in an overdense region and showed that hydrogen reionization was completed by galaxies, only at $z \sim 4$ radiation from black holes started to play an important role.

Here, we introduce a new simulation project, FOREVER22 (FORmation and EVolution of galaxies in Extremely-overdense Regions motivated by SSA22). In this project, we study galaxy evolution in protoclusters and the formation mechanism of observed galaxies, LAEs, LBGs, SMG, passive galaxies, and QSOs in the protoclusters at redshifts $z \geq 2$. Using a large volume of $(714 \text{ cMpc})^3$, we select the top 10 massive haloes and study the statistical properties of galaxies in them, baryonic physics and radiative properties. The FOREVER22 consists of three simulation sets with different resolutions and volumes: PCR (Proto-Cluster Region), BCG (Brightest proto-Cluster Galaxy), and First runs. By using these three series, we can investigate both the statistical nature and the small scale baryonic physics with stellar/AGN feedback.

Besides, we carry out multi-wavelength radiative transfer simulations that can calculate the properties of continuum flux from X-ray to radio, Lyman continuum, $\text{Ly}\alpha$, [OIII], [CII], CO lines. Thus, we can directly compare the simulations with recent observations with optical/NIR telescopes (e.g., Subaru, Keck, Hubble Space Telescopes) and radio telescopes (e.g., ALMA), and also predict for future missions (e.g., James Webb Space Telescope).

2 THE FOREVER22 SIMULATION

We utilize the SPH code GADGET-3 (Springel 2005) with the modifications developed in the *Overwhelmingly Large Simulations* (OWLS) project (Schaye et al. 2010). Following the EAGLE project (Schaye et al. 2015), we update the star formation and supernova (SN) feedback models. This code was also modified to handle the formation of population III (Pop III) stars, Lyman-Werner feedback, equilibrium primordial chemistry in the *First Billion Year* (FiBY) project (Johnson et al. 2013; Paardekooper et al. 2015). The new models as part of the FiBY project have been used to e.g. investigate the cosmic star-formation rate density of Pop III and Pop II stars, Lyman continuum leakage from high-redshift dwarf galaxies, dust extinction in high redshift galaxies, globular cluster formation and statistical

properties of direct-collapse black holes (e.g., Paardekooper et al. 2013; Agarwal & Khochfar 2015; Elliott et al. 2015; Cullen et al. 2017; Phipps et al. 2020). In this project, we add models to calculate the radiative feedback from young stars and kinetic feedback from massive black holes and the growth/destruction of dust grains.

The FOREVER22 project consists of three series of simulations: PCR, BCG, and First runs. Recent observational wide surveys reveal the large-scale structures around protoclusters (e.g., Kikuta et al. 2019), while at the same time high-angular resolution ALMA observations can resolve giant gas clumps or spiral arms in high-redshift galaxies (e.g., Tadaki et al. 2018). State-of-the-art simulations still struggle resolving both large-scale structures and small-scale gas clumps simultaneously. To overcome this limitation we designed the above mentioned runs to investigate the statistical properties of galaxies in protoclusters and their detailed structure evolution and feedback. The resolutions and parameters are summarised in Table 1 and more details on the individual runs will be given in the following sections.

• Proto-Cluster Region (PCR) runs

In the PCR runs, we consider $(28.6 \text{ cMpc})^3$ volumes to investigate the statistical nature of galaxies in protoclusters and the large-scale structures around them, where cMpc is comoving Mpc. The volume of the entire calculation box is $(714.2 \text{ cMpc})^3$. We choose the top 10 most massive haloes in the box at $z = 2$ and make zoom-in initial conditions with a side length of 28.6 cMpc. To highlight the effect of the environment we also choose three mean density regions and take the mean of them (MF run). We carry out hydrodynamics simulations down to $z = 2$ and study the statistical nature of galaxies and compare them with those in the mean density run. Figure 1 shows the gas distribution and positions of haloes with mass greater than $10^{12} M_{\odot}$. We find massive haloes form in nodes or cross points of large-scale filaments. The large-scale structures show variations. For example, PCR0 and PCR8 have a few thick filaments and the shapes look elongated. On the other hand, PCR4 and PCR7 consist of many thin filaments, and the shapes are isotropic. Unlike PCR regions, MF has only four massive haloes and no pronounced filaments are seen. In the case of major mergers between haloes, the peaks of the gas column density can be somewhat shifted from the centres of mass of haloes.

• Brightest proto-Cluster Galaxy (BCG) runs

To study gas dynamics in massive galaxies, we increase the mass resolution while at the same time the zoom-in region is limited to cover the most massive haloes only in each PCR region. The masses of gas and dark matter particles are 3.5×10^5 and $2.0 \times 10^6 h^{-1} M_{\odot}$ respectively, which are 8 times lower than in the PCR runs. We follow the evolution of the haloes down to $z = 4$ when they become massive with the stellar and black hole masses of $\gtrsim 10^{11}$ and $\gtrsim 10^8 M_{\odot}$. We also use the BCG runs to investigate the impact of stellar and AGN feedback on galaxy evolution.

• First galaxy (First) runs

The First runs are composed of two zoom-in simulations focusing on the formation of the first galaxies at $z \geq 9$. By

Halo ID	M_h [M_\odot/h] at $z_{\text{end}}(z=3)$	m_{gas} [M_\odot/h]	m_{DM} [M_\odot/h]	ϵ_{min} [kpc/h]	z_{end}
PCR0	1.9×10^{14} (8.1×10^{13})	2.9×10^6	1.6×10^7	2.0	2
PCR1	1.5×10^{14} (5.9×10^{13})	2.9×10^6	1.6×10^7	2.0	2
PCR2	1.2×10^{14} (5.6×10^{13})	2.9×10^6	1.6×10^7	2.0	2
PCR3	1.2×10^{14} (2.0×10^{13})	2.9×10^6	1.6×10^7	2.0	2
PCR4	1.1×10^{14} (3.8×10^{13})	2.9×10^6	1.6×10^7	2.0	2
PCR5	1.0×10^{14} (3.5×10^{13})	2.9×10^6	1.6×10^7	2.0	2
PCR6	9.9×10^{13} (4.6×10^{13})	2.9×10^6	1.6×10^7	2.0	2
PCR7	9.6×10^{13} (3.3×10^{13})	2.9×10^6	1.6×10^7	2.0	2
PCR8	9.1×10^{13} (5.1×10^{13})	2.9×10^6	1.6×10^7	2.0	2
PCR9	9.1×10^{13} (2.0×10^{13})	2.9×10^6	1.6×10^7	2.0	2
MF	1.4×10^{13} (6.1×10^{12})	2.9×10^6	1.6×10^7	2.0	2
BCG0	2.0×10^{13}	3.5×10^5	2.0×10^6	1.0	4
BCG1	2.9×10^{13}	3.5×10^5	2.0×10^6	1.0	4
BCG2	2.8×10^{13}	3.5×10^5	2.0×10^6	1.0	4
BCG3	5.4×10^{12}	3.5×10^5	2.0×10^6	1.0	4
BCG4	2.0×10^{13}	3.5×10^5	2.0×10^6	1.0	4
BCG5	1.8×10^{13}	3.5×10^5	2.0×10^6	1.0	4
BCG6	1.7×10^{13}	3.5×10^5	2.0×10^6	1.0	4
BCG7	9.1×10^{12}	3.5×10^5	2.0×10^6	1.0	4
BCG8	1.5×10^{13}	3.5×10^5	2.0×10^6	1.0	4
BCG9	6.0×10^{12}	3.5×10^5	2.0×10^6	1.0	4
BCG0noAGN	2.0×10^{13}	3.5×10^5	2.0×10^6	1.0	4
BCG0spEdd	2.0×10^{13}	3.5×10^5	2.0×10^6	1.0	4
First0	3.5×10^{11}	5.5×10^3	3.1×10^4	0.2	9.5
First1	3.2×10^{11}	5.5×10^3	3.1×10^4	0.2	9.5

Table 1. Parameters of zoom-in cosmological hydrodynamic simulations: (1) M_h is the halo mass at the final redshift (z_{end}). (2) m_{gas} is the initial mass of gas particles. (3) m_{DM} is the dark matter particle mass. (4) ϵ_{min} is the gravitational softening length in comoving units.

making zoom-in initial conditions covering the most massive haloes in PCR0 and PCR1 regions at $z = 9.5$, we increase the mass resolutions of gas and DM to 5.5×10^3 and $3.1 \times 10^4 h^{-1} M_\odot$, which can resolve mini-haloes hosting Pop III stars. In the First runs in contrast to the other runs we also consider non-equilibrium chemistry of primordial gas to follow the gas collapse in the mini-haloes via H_2 cooling.

The FiBY project, Johnson et al. (2013) presented the cosmic star formation rate densities of Pop III and Pop II stars in a mean density environment. Due to the metal enrichment, Pop II star formation becomes dominant at $z \lesssim 10$. In our runs the transition from Pop III to Pop II stars likely occurs earlier than in the mean-density FiBY runs due to rapid metal enrichment via type-II supernovae (SNe). Using the First runs, we study the metal enrichment in protocluster regions and formation of first galaxies with Pop II stars. Also, upcoming telescopes, e.g., James Webb Space Telescope (JWST) aim at detecting the first galaxies at $z \gtrsim 10$. Since galaxies in the over-dense regions are likely to have a high star formation rate (SFR), they can be plausible candidates for future observations. Therefore we investigate the brightness and observability of the first galaxies in PCs.

We use a friend-of-friend (FOF) group finder to identify haloes on-the-fly. In massive haloes, there are some satellite galaxies. We utilize SUBFIND (Springel 2005) to identify member galaxies in haloes in post-processing. We adopt following cosmological parameters that are consistent with the current cosmic microwave background observations: $\Omega_M = 0.3$, $\Omega_b = 0.045$, $\Omega_\Lambda = 0.7$, $n_s = 0.965$, $\sigma_8 = 0.82$, and

$h = 0.7$ (Komatsu et al. 2011; Planck Collaboration et al. 2016, 2020).

2.1 Star Formation

We follow a star formation (SF) model developed in Schaye & Dalla Vecchia (2008) which was used in OWLS and EAGLE projects. This SF model is based on the Kennicutt-Schmidt law of local galaxies, i.e., SFR surface density is proportional to gas surface density. Schaye & Dalla Vecchia (2008) assume the disk scale height to be equal to the Jeans length and model the local SFR based on the local ISM pressure:

$$\dot{m}_* = m_g A (1 M_\odot \text{ pc}^{-2})^{-n} \left(\frac{\gamma}{G} f_g P \right)^{(n-1)/2}, \quad (1)$$

where m_g is the mass of the gas particle, $\gamma = 5/3$ is the ratio of specific heats, f_g is the gas mass fraction in the self-gravitating galactic disc, and P is the total ISM pressure. The free parameters in this SF model are the amplitude A and the power-law index n . These parameters are related to the Kennicutt-Schmidt law,

$$\dot{\Sigma}_* = A \left(\frac{\Sigma_{\text{gas}}}{1 M_\odot \text{ pc}^{-2}} \right)^n. \quad (2)$$

Local normal star-forming galaxies follow $A_{\text{local}} = 2.5 \times 10^{-4} M_\odot \text{ yr}^{-1} \text{ kpc}^{-2}$ and $n = 1.4$ for a Salpeter IMF (Kennicutt 1998). Note that, the amplitude should be changed by a factor $1/1.65$ in the case of the Chabrier IMF, i.e., $A_{\text{local,Chab}} = 2.5 \times 10^{-4} M_\odot \text{ yr}^{-1} \text{ kpc}^{-2}$. Schaye et al. (2010) reproduced the observed cosmic star formation rate density

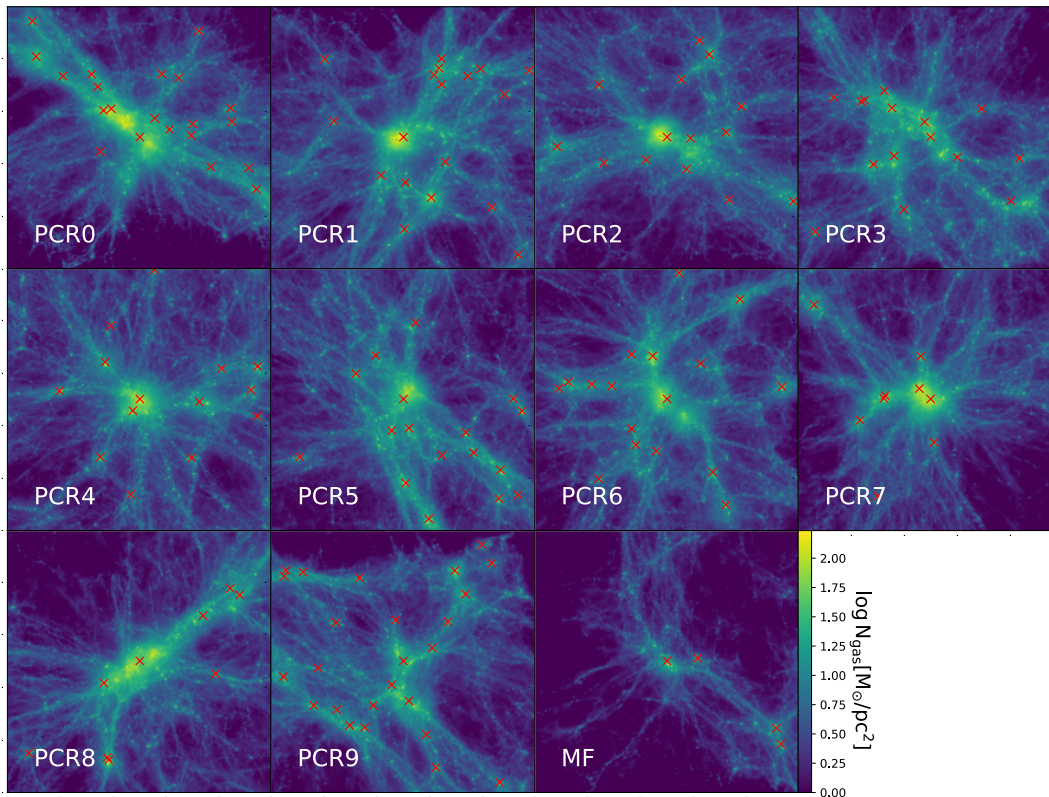


Figure 1. Gas structures in PCR and MF runs at $z = 3$. The color represents gas column density with thickness of 10 cMpc. The box size is 10 cMpc \times 10 cMpc. Red crosses indicate the centre of mass of massive haloes with $M_h \geq 10^{12} M_\odot$.

(SFRD) using cosmological SPH simulations with this SF model and the parameters $A = 1.5 \times 10^{-4} M_\odot \text{ yr}^{-1} \text{ kpc}^{-2}$ and $n = 1.4$ (see also, Schaye et al. 2015). As in EA-GLE, we change the slope n to 2.0 for high-density gas with $n_H > 10^3 \text{ cm}^{-3}$ and use the threshold density depending on local metallicity as $n_H = n_0 \text{ cm}^{-3} \left(\frac{Z}{0.002}\right)^{-0.64}$ where we set $n_0 = 0.1$ for PCR and BCG runs and 10.0 for First runs.

For gas at densities $n_H > n_0$, we use an effective equation of state with an effective adiabatic index $\gamma_{\text{eff}} = 4/3$. The floor temperatures at $n_H = n_0$ are 8000 K for PCR and BCG runs and 1000 K for First runs.

In BCG and First runs, we follow Pop III star formation. If the gas phase metallicity of star forming gas is lower than $1.5 \times 10^{-4} Z_\odot$ (Bromm & Loeb 2003; Omukai et al. 2005), Pop III stars form with an initial mass function (IMF) $dn \propto M^{-2.35} dM$ within the mass range 10 – 500 M_\odot . Due to the higher typical stellar mass, Pop III stars give strong feedback to the surrounding gas and induce metal enrichment rapidly. Since we set a minimum mass of 10 M_\odot , all Pop III stars will end as SNe or direct collapse BHs. Therefore, we do not consider energetic feedback and metal pollution via Type Ia SNe and the AGB phase from Pop III stars. Some Pop III

stars are likely to be single stellar-mass BHs or high-mass X-ray binaries (HMXBs) at the end of their lifetime and will suppress star formation in the first galaxies (e.g., Jeon et al. 2014). In this work, we do not take remnant BHs and HMXBs into account.

2.2 UV background radiation

As the cosmic star formation rate density (CSFRD) increases, the universe is filled with UV background (UVB) radiation (Haardt & Madau 1996; Haardt & Madau 2001; Faucher-Giguère et al. 2009). The UVB heats the intergalactic medium (IGM) and changes the ionization states of primordial gas and metals. The cooling rate is estimated from the assumption of equilibrium (collisional or photoionization) for each metal species. The metal-line cooling is considered for each metal species using a pre-calculated table by CLOUDY v07.02 code (Ferland 2000). At $z \lesssim 10$, galaxies are irradiated by the UVB, and it penetrates into the gas with $n_H < 0.01 \text{ cm}^{-3}$ which is the threshold density for self-shielding as derived by Nagamine et al. (2010) and Yajima et al. (2012a) based on the radiative transfer calculations

of the UVB. We switch from collisional to photoionization equilibrium cooling tables once the UVB ionizes the gas (see Johnson et al. 2013, for details). We use the UVB of Haardt & Madau (2001) in our simulations. The clustering of galaxies and the high star formation activity in the protocluster regions can boost the local UV radiation field. In this work, we do not take into account local fluctuations of the UVB.

2.3 Stellar Radiation Feedback

• Photo-ionization feedback

We take account of feedback from stars by considering the photo-ionization heating and radiation pressure on dust. This radiative feedback mainly originates from young star clusters. Therefore, in this work, we take stellar particles with an age of ≤ 10 Myr into account as the sources of the radiative feedback. We assume a black-body spectrum with $T = 10^5$ K for Pop III stars and a synthesized sed with a Chabrier IMF with zero age for Pop II stars, and estimate the photon production rate from a stellar particle. Once the stellar age exceeds 10 Myr, we turn off the radiative feedback and then consider supernova feedback as explained below.

The photo-ionization heats the gas to $\gtrsim 10^4$ K, resulting in the expansions of HII bubbles due to the higher thermal pressure if the pressure of surrounding gas is lower. We estimate the ionized region by solving the balance between the ionizing photon production rate (\dot{N}_{ion}) from young star-clusters and the total recombination rate of the ionized gas as:

$$\dot{N}_{\text{ion}} = \sum_{i=1}^n \alpha_{\text{B}} n_{\text{HII}}^i n_{\text{e}}^i \frac{m_{\text{gas}}^i}{\rho_{\text{gas}}^i}, \quad (3)$$

where \dot{N}_{ion} is the photon production rate of a stellar particle, α_{B} is the case-B recombination coefficient, n_{HII}^i and n_{e}^i are the ionized hydrogen and electron number densities of i -th SPH particle. In the ionized region, we set $n_{\text{HII}} = n_{\text{e}} = n_{\text{H}}$, where n_{H} is the total hydrogen number density. Here we evaluate the volume by the gas mass of i -th SPH particle m_{gas}^i and its mass density ρ_{gas}^i . We sum up the total recombination rate of the surrounding gas from the nearest gas particle ($i = 1$) in turn. If there are several stellar particles in a small area, the ionized regions can overlap each other and make larger ionized bubbles. In this work, we do not consider the overlap effect. The temperature of the ionized gas is set to $T_{\text{HII}} = 3 \times 10^4$ K. The temperature of ionized regions can change between $\sim 1 \times 10^4 < T_{\text{HII}} < \sim 3 \times 10^4$ K depending on the stellar metallicity. We consider the case of very low-metallicity or Pop III stars. Note that, in the case of PCR and BCG, the pressure of high-density regions can be higher than the case considering T_{HII} because of the effective equation-of-state (EoS) model. Therefore, the photo-ionization heating works only for the low-density environments at $n_{\text{H}} \lesssim 5 \text{ cm}^{-3}$. If the recombination rate of the nearest gas-particle alone is higher than \dot{N}_{ion} , only the nearest particle is recognized as in the ionized region. We prohibit the star formation in the ionized region.

• Radiation pressure on dust

A part of UV radiation from young stars is absorbed by dust, which gives outward momentum to gas (e.g., Murray

et al. 2005; Yajima et al. 2017b). We here estimate the mean free path of UV continuum photons in dusty gas as $l_{\text{m.f.p}} = \frac{1}{\kappa_{\text{d}} \rho_{\text{gas}}}$, where κ_{d} is the absorption coefficient. Here we set $\kappa_{\text{d}} = 2.5 \times 10^2 \text{ cm}^{-2} \text{ g}^{-1} (Z/Z_{\odot})$, which is corresponding to the silicate dust with the size of $\sim 0.1 \mu\text{m}$ and the dust-to-gas mass ratio of ~ 0.01 corresponding to solar abundance. Within $l_{\text{m.f.p}}$, we can assume to be in the optically thin limit and estimate the radiation force as

$$\mathbf{F}_{\text{rad}} = \frac{\rho_{\text{gas}} \kappa_{\text{d}} L_{\text{UV}}}{4\pi r^2 c} \frac{\mathbf{r}}{r}, \quad (4)$$

where L_{UV} is the UV luminosity. We estimate L_{UV} by integrating the SED of a stellar particle from $\lambda = 1000 - 5000 \text{ \AA}$, which is the range that radiation is efficiently absorbed by dust.

• Hydrogen molecule dissociation

In the case of First runs, we consider the dissociation process of hydrogen molecules due to Lyman-Werner (LW) feedback (Johnson et al. 2013). Here we consider H_2 dissociation and H^- detachment due to local radiation sources. The LW mean intensity is estimated by

$$J_{\text{LW},21} = \sum_{i=1}^n f_{\text{LW}} \left(\frac{r_i}{1 \text{ kpc}} \right)^{-2} \left(\frac{m_{*,i}}{10^3 M_{\odot}} \right), \quad (5)$$

where $J_{\text{LW},21}$ is described in unit of $10^{-21} \text{ erg s}^{-1} \text{ cm}^{-2} \text{ Hz}^{-1} \text{ str}^{-1}$, r_i is the distance from i -th stellar particle to a target gas particle and $m_{*,i}$ is the mass of i -th stellar particle. The normalization factor f_{LW} depends on the shape of SEDs. However, Sugimura et al. (2017) showed that the feedback strength of young Pop II stars per unit mass was similar to that of Pop III stars (see also Agarwal et al. 2016). Therefore, unlike Johnson et al. (2013), we use the same value to both Pop III and II stars, and it is $f_{\text{LW}} = 15$. The LW radiation can be attenuated locally due to self-shielding gas (e.g., Draine & Bertoldi 1996; Glover & Brand 2001; Wolcott-Green et al. 2011, 2017; Luo et al. 2020). To take the self-shielding effect into account, we evaluate the column density over the local Jeans length as follows:

$$N_{\text{H}_2} = 2 \times 10^{15} \text{ cm}^{-2} \left(\frac{f_{\text{H}_2}}{10^{-6}} \right) \left(\frac{n_{\text{H}}}{10 \text{ cm}^{-3}} \right)^{1/2} \left(\frac{T}{10^3 \text{ K}} \right)^{1/2}, \quad (6)$$

with f_{H_2} is the fraction of H_2 , n_{H} is the hydrogen number density. Using the column density, we estimate the shielding factor based on Wolcott-Green et al. (2011) as

$$f_{\text{shield}}(N_{\text{H}_2}, T) = \frac{0.965}{(1 + x/b_5)^{1.1}} + \frac{0.035}{(1 + x)^{0.5}} \times \exp[-8.5 \times 10^{-4} (1 + x)^{0.5}], \quad (7)$$

where $x \equiv N_{\text{H}_2}/5 \times 10^{14} \text{ cm}^{-2}$ and $b_5 \equiv b/10^5 \text{ cm s}^{-1}$. Here b is the Doppler broadening parameter, $b \equiv (k_{\text{B}}T/m_{\text{H}})^{1/2}$. Thus, we estimate the H_2 dissociation rate by combining $J_{\text{LW},21}$ and f_{shield} . Once stars form in a halo, star formation in some nearby minihalos is suppressed due to the LW feedback (e.g., Latif et al. 2020). As the halo mass increases or gas is metal-enriched, gas can collapse via metal cooling or hydrogen atomic cooling.

2.4 Supernova Feedback

In this work, we consider supernovae (SNe) feedback via the injection of thermal energy into neighboring gas particles as described in Dalla Vecchia & Schaye (2012). Using random numbers, gas particles are chosen stochastically and heated up to $T = 10^{7.5}$ K. The hot gas region pushes out the surrounding ISM due to the higher thermal pressure. This can lead to galactic-scale outflow if the thermal energy is converted to kinetic energy efficiently. The conversion rate depends on the local physical properties, e.g., gas density, clumpiness, metallicity (e.g., Cioffi et al. 1988; Kim & Ostriker 2015). Dalla Vecchia & Schaye (2012) compared the sound crossing time with the cooling time, and derived the following maximum gas density for which the thermal energy is efficiently converted into the kinetic energy against radiative cooling losses:

$$n_{\text{H}} \sim 100 \text{ cm}^{-3} \left(\frac{T}{10^{7.5} \text{ K}} \right)^{3/2} \left(\frac{m_{\text{g}}}{10^4 M_{\odot}} \right)^{-1/2}. \quad (8)$$

Some star-forming regions can exceed the above critical density and suffer from the over-cooling problem. Also, in regions with lower metallicity and lower gas density, the SN explosion energy is easier converted into kinetic energy due to lower cooling rates (e.g., Cioffi et al. 1988; Thornton et al. 1998). Therefore, as introduced in S15, we consider a multiplication factor (f_{th}) to the SN energy depending on local metallicity and gas density as

$$f_{\text{th}} = f_{\text{th,min}} + \frac{f_{\text{th,max}} - f_{\text{th,min}}}{1 + \left(\frac{Z}{0.1 Z_{\odot}} \right)^{n_z} \left(\frac{n_{\text{H,birth}}}{n_{\text{H,0}}} \right)^{-n_n}}, \quad (9)$$

where $n_{\text{H,birth}}$ is the gas density at which the star particle is formed, $n_z = n_n = 2/\ln(10)$, and $n_{\text{H,0}} = 0.67 \text{ cm}^{-3}$, which were chosen after the comparison tests in S15. We here use the asymptotic values $f_{\text{th,max}} = 2.5$ and $f_{\text{th,min}} = 0.3$. As discussed in S15, f_{th} can exceed unity. This is motivated by the additional feedback processes, not included in the simulations, e.g., stellar winds, cosmic rays, or if supernova yield more energy per unit mass than assumed here. Since we consider radiative feedback from young stars, we use a somewhat lower value of $f_{\text{th,max}}$ than S15 ($f_{\text{th,max}} = 3.0$). Crain et al. (2015) discuss that the dependencies of the CSFRD and other properties of simulated galaxies on the choice of f_{th} . They concluded that the above model of f_{th} reproduced the observations of local galaxies well. The resolution of the PCR runs can allow a maximum density of $n_{\text{H}} \sim 5 \times 10^3 \text{ cm}^{-3}$. Therefore, such a high-density region can still suffer from the over-cooling, although it is rare.

2.5 Black hole

As galaxies evolve, massive black holes (BHs) are likely to form at the galactic centers (e.g., Kormendy & Ho 2013). Massive BHs can suppress star formation via radiative and kinetic feedbacks (e.g., Dubois et al. 2012). Recent simulations show that star formation in massive galaxies can be suppressed by BH feedback to reproduce the stellar-to-halo-mass ratio (SHMR; e.g., Pillepich et al. 2018b). To account for this we include BH feedback in our simulations. We put a BH with a mass of $10^5 M_{\odot}/h$ at the galactic center if the halo once its mass exceeds $10^{10} M_{\odot}/h$. Gas accretion rate

on the BHs is estimated based on the Bondi rate (Bondi & Hoyle 1944) using neighbor gas particles as

$$\dot{m}_{\text{Bondi}} = \frac{4\pi cGM_{\text{BH}}^2 \rho}{(c_s^2 + v_{\text{rel}}^2)^{3/2}} \quad (10)$$

where v_{rel} is the relative velocity between the BH particle and gas particle. As in S15, we consider a suppression factor due to angular momentum of gas,

$$\dot{m}_{\text{acc}} = \dot{m}_{\text{Bondi}} \times \min(C_{\text{visc}}^{-1} (c_s/V_{\phi})^3, 1) \quad (11)$$

where C_{visc} is a free parameter related to the viscosity of subgrid accretion disc (Rosas-Guevara et al. 2015). We set $C_{\text{visc}} = 200\pi$ which is same as in the AGNdT9 run in S15, which has been shown to reproducing the observed X-ray luminosity function well (Rosas-Guevara et al. 2016). BHs grow with the rate $\dot{m}_{\text{BH}} = (1 - f_r)\dot{m}_{\text{acc}}$ where $f_r = 0.1$ is the radiative efficiency factor. The simulations suffer from resolving high-density gas within the Bondi radius. By taking the balance between the Bondi rate without the relative velocity and the Eddington accretion rate ($\dot{m}_{\text{Edd}} = L_{\text{Edd}}/(f_r c^2)$), we evaluate the gas density around a BH that would allow for Eddington accretion (Park & Ricotti 2011; Yajima et al. 2017b)

$$\begin{aligned} n_{\text{H}} &\sim \frac{c_s^3}{G\sigma_{\text{TC}}f_r M_{\text{BH}}} \\ &\sim 40 \text{ cm}^{-3} \left(\frac{M_{\text{BH}}}{10^5 M_{\odot}} \right)^{-1} \left(\frac{T_{\text{gas}}}{10^4 \text{ K}} \right)^{1.5} \left(\frac{f_r}{0.1} \right)^{-1}. \end{aligned} \quad (12)$$

Therefore some previous studies with low numerical resolutions had to introduce a boost factor to the accretion rate. On the other hand, the numerical resolutions of recent simulations can follow the accumulation of high-density gas around BHs, resulting in the efficient growth of BHs without the boost factor, e.g., as in S15. Also, our simulations follow the growth of BHs without the boost factor and reproduce the formation of SMBHs in massive galaxies successfully, of which the masses distribute near the local relation between the BH and stellar-bulge mass. In our fiducial model, we set the upper limit of the accretion rate as the Eddington limit,

$$\dot{m}_{\text{Edd}} = \frac{4\pi GM_{\text{BH}} m_{\text{p}}}{f_r \sigma_{\text{TC}}}. \quad (13)$$

In the current resolution, it is difficult to follow the migration process of BHs due to dynamical friction. We therefore artificially model the migration of BHs toward the galactic centers by replacing them to the position of the potential minimum of neighbouring particles. Once the BH settles at a galactic center, it starts to grow efficiently. Then, the growth can be self-regulated via feedback from the BH. In this work, we consider two types of feedback processes as described below.

- *Quasar mode feedback*

The energy from an accretion disk is deposited into neighbouring gas particles thermally. The released energy is estimated by $\Delta E = f_e f_r \dot{m}_{\text{acc}} c^2$, where f_e is the thermal coupling factor. Here we assume $f_e = 0.15$ and $f_r = 0.1$ for the large-scale simulations (PCR series). Unlike S15, we choose the nearest gas-particle and inject the thermal energy. If thermal energy injection occurs continuously, the next gas particles are selected in order of the distance from

the BH.

- *Radio mode feedback*

As observed radio galaxies, supermassive black holes (SMBHs) with the mass $\sim 10^9 M_\odot$ are likely to have impact on galactic scale via jet-like kinetic feedback. We therefore, inject half of ΔE as kinetic energy and the other as thermal energy, once the BH mass exceeds $10^9 M_\odot$. We add the momentum to the gas kicked in the radio mode feedback to follow the direction of the angular momentum vector of neighbouring gas particles or the opposite direction, and the kick velocity is 3000 km s^{-1} . The direction of the kick velocity is set along the angular momentum vector of surrounding gas $\mathbf{n}_1 = \mathbf{L}/|L|$ or the inverse direction $\mathbf{n}_2 = -\mathbf{L}/|L|$. We determine either direction via random numbers.

- *Super-Eddington mode*

Recent simulations show that disc winds can be launched due to the radiation from the inner parts of an accretion disc (e.g., Murray et al. 1995; Proga et al. 2000; Proga & Kallman 2004; Nomura et al. 2020). This disc wind can obscure the radiation from the accretion disc and generate an anisotropic radiation field. In the case of an anisotropic radiation field, the gas accretion rate onto BHs can simply be proportional to the Bondi rate and not capped at the Eddington limit (e.g., Netzer 1987; Wada 2012; Sugimura et al. 2017). Therefore, only for the run BCG0spEdd, we allow super-Eddington accretion, but set the maximum Eddington factor $f_{\text{Edd}} = 5$. When the accretion rate exceeds the Eddington accretion rate, the radiative efficiency can be low due to the photon trapping in a slim disk (e.g., Jaroszynski et al. 1980). We evaluate the luminosity of BHs based on a fitting formula (Watarai et al. 2000),

$$L = \begin{cases} 2.0L_{\text{Edd}} [1 + \ln(\frac{\dot{m}}{2.0})] & \text{if } \dot{m} > 2.0 \\ L_{\text{Edd}}\dot{m} & \text{if } \dot{m} \leq 2.0, \end{cases} \quad (14)$$

where $\dot{m} \equiv \dot{m}_{\text{acc}}/\dot{m}_{\text{Edd}}$ is the gas accretion rate normalized by the Eddington accretion rate and L_{Edd} is the Eddington luminosity $L_{\text{Edd}} = 4\pi cGM_{\text{BH}}m_p/\sigma_T$.

2.6 Post-processing radiative transfer

To study the observational properties of simulated galaxies, we carry out post-processing radiative transfer calculations for specific snapshots. We use the multi-wavelength radiative transfer code ART² (Li et al. 2008, 2020; Yajima et al. 2012c). This code is developed based on a Monte Carlo technique and calculates the transfer of photon packets through an adaptive refinement grid structure. The newest version of ART² can handle continuum fluxes from stars and black holes, Ly α line from ionized hydrogen, atomic metal lines, and CO lines. Moreover, the code can make two-dimensional images of surface brightness for specific frequency ranges. Using the code, we reproduced successfully observational properties of high-redshift galaxies (Yajima et al. 2012b, 2013, 2014, 2015a,b; Arata et al. 2019, 2020). We will model the observational properties of member galaxies of PCs in the next papers. In this work, we study the dust obscuring of massive galaxies in the PCs and infrared luminosities from the dust thermal emission. By considering the radiative

equilibrium state, we estimate the dust temperature locally and the flux densities at far-infrared wavelengths.

The adaptive refinement grid structures for the radiative transfer simulations are set to resolve the minimum smoothing length ($0.1 \times$ gravitational softening). The physical properties of each grid are estimated from neighbouring SPH particles with a spline kernel function and a smoothing length. Using the local metallicity, we model the dust density as $\rho_d = 8 \times 10^{-3} \rho_{\text{gas}}(Z/Z_\odot)$. This relation is supported by observation of local galaxies (e.g., Draine et al. 2007). We cast 10^6 photon packets, which satisfies our convergence checks and generate good resolution SEDs.

3 RESULTS

3.1 PCR runs

Figure 2 shows the distributions of gas, metallicity, and stars of the most massive halo in the PCR0 run and the large-scale structure at $z = 3$. As seen in the stellar distribution, the massive galaxies are undergoing a major merger. The total stellar mass and star formation rate in the halo are $2.5 \times 10^{12} M_\odot$ and $2679 M_\odot \text{ yr}^{-1}$, respectively. The central parts of the galaxies already reach solar metallicity.

Figure 3 presents the total SFRs within a radius of 10 cMpc, which corresponds to a typical Lagrange volume of PCs at $\gtrsim 2$ that makes clusters at $z \sim 0$ (e.g., Chiang et al. 2017). The centre of the proto-cluster region is chosen as the centre of mass of all massive galaxies with $M_h \geq 10^{12} M_\odot$ in the zoom-in regions ($L = 28.6 \text{ Mpc}$). The total SFRs monotonically increase with time at $z \gtrsim 4$ and then stall or somewhat decrease from $z = 4$ to 2. The evolution of the star formation histories differs from the cosmic star formation rate density (SFRD) as seen for the mean-field (MF) run or as derived from observations (Madau & Dickinson 2014) in which the peak of SFRD is at $z \sim 1 - 3$. In the PC regions, massive galaxies consume gas via star formation earlier and the overall gas fraction becomes small at $z < 4$, resulting in a suppression of star formation activities. In addition, SMBHs form in the massive galaxies and hamper star formation via feedback. Note that, however, the star formation in massive galaxies is not quenched for a long time. Most of them can keep gas and maintain star formation, which will be discussed below.

Most of the PCR runs show a total SFR of $\sim 3000 - 5000$ at $z = 2 - 4$. Only PCR0 exceed that with $6000 M_\odot \text{ yr}^{-1}$ at $z = 2 - 4$ and achieves $9378 M_\odot \text{ yr}^{-1}$ at $z = 3.5$. The PCRs agree with the lower end of observed SFRs in PCs at $z \lesssim 3$ (Lacaille et al. 2019), with some observed PCs being a factor of 2 - 3 higher. Note that, however, the estimate of the SFRs of observed PCs always suffers from the uncertainties of the dust temperature and the contribution of hidden AGNs. Kubo et al. (2019) suggested that the total SFR of the PC they observe at $z = 3.8$ could be boosted due to the additional submillimeter flux from the dust-obscured AGN by an order unity. Also, in the observations, the field of view and the detection limits are not uniform. The dependency on the observed sky-area is discussed below.

The PC regions show total SFRs of $> 1000 M_\odot \text{ yr}^{-1}$ even at $z \sim 6 - 8$. Such high star formation rate will be accompanied with copious amounts of ionizing photons. There-

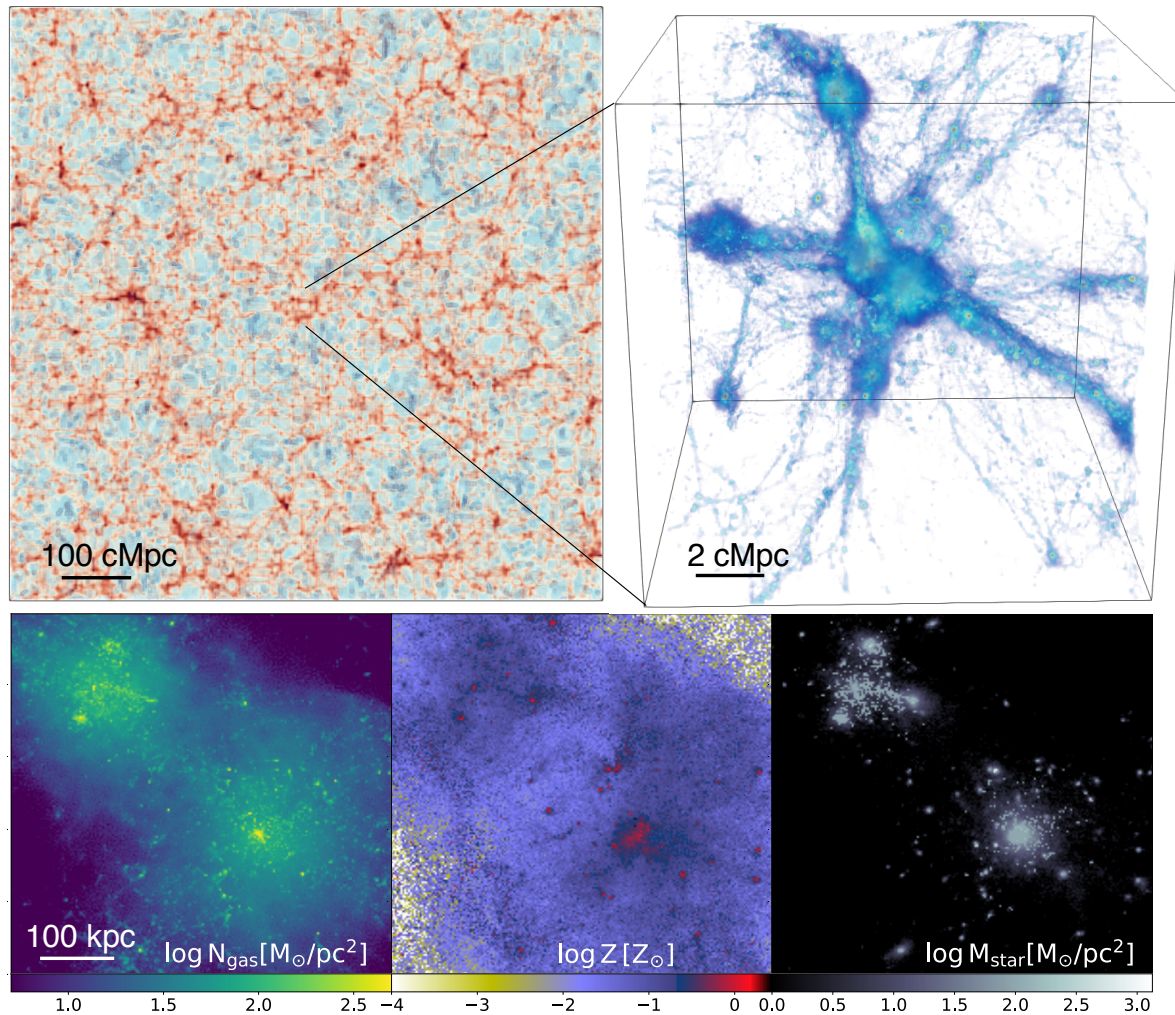


Figure 2. Upper left: The large scale structure of matter in the entire calculation box with $L = 714$ cMpc. Upper right: Three-dimensional gas structure of the PCR0 region at $z = 3$. Lower panels: Gas column density (left), density-weighted metallicity (middle) and stellar surface density (right) of the most massive halo in PCR0.

fore these starburst regions are likely to induce cosmic reionization much earlier and make giant HII bubbles that have high IGM transmission of Ly α lines from galaxies in the bubbles (Yajima et al. 2018). We will investigate the relation between giant H II bubbles and the clustering of LAEs at the epoch of reionization in a follow-up study.

As shown in Miller et al. (2018), the concentration of starburst galaxies can be an important factor characterizing PCs. Figure 4 shows the cumulative SFR within a specific sky-area. Here, we choose the most massive galaxy as the centre and integrate the SFR as a function of 2D radial distance with the projection depth of 28.6 cMpc. The simulations show that the cumulative SFR increases significantly at $10^7 - 10^8$ kpc 2 . The most massive halo in PCR0 hosts five galaxies with SFR > 100 $M_{\odot} \text{ yr}^{-1}$ and there are seven starburst galaxies in the zoom-in region. Most other PCRs also have more than five galaxies with SFR > 100 $M_{\odot} \text{ yr}^{-1}$ in the zoom-in regions. We find that the SFRs of all PCRs do not exceed 3000 $M_{\odot} \text{ yr}^{-1}$ at $\lesssim 10^7$ kpc 2 . This is because the typical separation distance between massive haloes is

~ 1 cMpc as seen in Figure 1, which requires at least a sky-area with $\sim 10^7$ kpc 2 to include a second massive halo with high SFR. Some observed PCs also show a similar trend to the one reported in our simulations (e.g., Casey et al. 2015). Whereas, even PCR0 cannot reach the high SFR of SSA22 which exceed 10^4 $M_{\odot} \text{ yr}^{-1}$ within 10^8 kpc 2 . This may indicate that SSA22 is a more high-density rare peak or the SFR is overestimated because of a hidden AGNs. Alternatively, the current simulation underestimates the SFR of massive haloes in PCs regions. Recently, Lim et al. (2020) indicated that the SFR of simulated PCs increases significantly with the resolution of the simulations. Furthermore, two protoclusters, SPT2349-56 (Miller et al. 2018) and S004224 (Oteo et al. 2017), show highly concentrated star formation activity. These protoclusters reach ~ 6000 $M_{\odot} \text{ yr}^{-1}$ even within 10^5 kpc 2 which is much higher than in other observed protoclusters and our simulations. For example, SPT2349-56 shows more than 10 starburst galaxies with SFR $\gtrsim 100$ $M_{\odot} \text{ yr}^{-1}$ coexisting within a small area.

Cosmic star formation rate densities (SFRD) are pre-

sented in Figure 5. The SFRD of the MF run roughly matches the observations. Earlier work has shown that the SFRD is regulated by SNe feedback (e.g., Schaye et al. 2010). As structure formation proceeds, haloes grow via mergers and matter accretion. Therefore the total star formation rate in the simulation volume increase. As the redshift decreases, the halo growth rate decreases gradually, and gas in galaxies is consumed by star formation, resulting in the plateau of SFRD $z \sim 2 - 3$. At $z \gtrsim 6$, there is large uncertainty in observed SFRDs. Oesch et al. (2015) indicates that the SFRD drops down significantly at $z > 6$, while a recent survey of dusty star-forming galaxies with ALMA shows a higher SFRD (Gruppioni et al. 2020; Khusanova et al. 2020). The SFRD of the MF run lies between reported results from galaxy observations in the UV and rest frame infrared. Note that, the SFRD in simulations sensitively depends on the feedback model and resolution as shown in Schaye et al. (2010), because low-mass haloes are significant contributors. In the MF run, the impact of AGN feedback is secondary, it reduces SFRD at $z \lesssim 3$ by at most a factor of 2.

SFRDs in the PCR runs are higher than that of the MF run by a factor of $\sim 3 - 5$. These differences are higher than the differences of total matter mass included in haloes in the zoom-in regions. In the overdense regions, more massive haloes form, and the halo number density is larger than in the mean-density field, leading to higher SFRDs. The shapes of the SFRDs of the PCR 1-4 runs are similar to that of the MF run, with the only difference that the normalisation is higher. On the other hand, PCR0 shows a slight decrease from $\sim 0.4 M_{\odot} \text{ yr}^{-1} \text{ Mpc}^{-3}$ at $z = 4$ to $\sim 0.3 M_{\odot} \text{ yr}^{-1} \text{ Mpc}^{-3}$ at $z = 2$. This is due to AGN feedback. Some massive haloes host SMBHs with $\sim 10^9 M_{\odot}$ at $z \lesssim 5$ which suppress star formation.

Figure 6 shows stellar mass functions at $z = 2, 3, 4$ and 7. We consider the total stellar masses of all galaxies identified by SUBFIND. The MF run successfully reproduces the observed stellar mass functions at $z = 2 - 7$. This indicates that the sub-grid models in our simulations are tuned reasonably (see e.g. also Cullen et al. 2017). The PCR runs always show stellar mass functions with large normalization ϕ that is higher by a factor $\sim 1 - 3$. The total matter masses included in all haloes in PC runs are higher than MF by a factor of $\sim 2 - 3$. As a reference, we add the stellar mass functions of MF boosted by a factor of 2.5 artificially. At $z \gtrsim 4$, it is similar to the PCR runs. On the other hand, at lower redshift $z \lesssim 4$, the stellar mass functions of the PCR runs become smaller than the boosted one at $M_{\text{star}} \lesssim 10^9 M_{\odot}$, while the tails at the massive end are building up. At $z = 2$, the massive ends of the PCRs reach $\sim 10^{12} M_{\odot}$, while ϕ at the low-mass end $\lesssim 10^{10} M_{\odot}$ becomes smaller than the dashed line significantly. This indicates that massive haloes form at the cores of PCs and contribute to the mass enhancement in the regions.

The relation between SFR and stellar mass is used as a ruler of star formation activity. As in Pillepich et al. (2018b,a), we estimate the gas/stellar mass and SFR within $2 \times r_{0.5}$, where $r_{0.5}$ is the half mass radius of stars in the most massive member galaxy in a halo. These physical quantities will also be used in next figures. Figure 7 shows the SFRs as a function of stellar mass. We find most galaxies distribute along the observed main-sequence lines even in the

PC regions at $z \gtrsim 2$. Hayashi et al. (2016) suggested that observed massive galaxies in a protocluster at $z = 2.5$ were on the main-sequence (but see, Shimakawa et al. 2018). Also, this is in agreement with results presented by Sparre et al. (2015) who showed that most galaxies distributed along the main sequence at $z > 1$ in their simulation and that massive galaxies with $M_{\text{star}} \gtrsim 10^{11} M_{\odot}$ only get quenched at $z < 1$. Note that the total stellar masses of some galaxies identified by SUBFIND are somewhat higher than the values estimated by the above method. However, the trend in the figure does not change significantly. The values can move to higher SFR and stellar mass along the main-sequence line in the case of using the stellar mass of the galaxies slightly. On the other hand, observations indicate some massive galaxies should be quenched even at $z \sim 2$ (Daddi et al. 2005; Tacchella et al. 2015; Tanaka et al. 2019; Esdaile et al. 2020). The quenching of star formation in massive galaxies can be induced by AGN feedback. In the current simulations of galaxy formation, the gas structure near the central BHs and their feedback are not well resolved. Therefore, various sub-grid models for gas accretion and feedback have been developed (Dubois et al. 2012; Schaye et al. 2015; Nelson et al. 2018), and those models for massive galaxies are still under debate.

We find that the distribution of SFR in the PCR runs does not differ from that in the MF run. This suggests that star formation activity may not be sensitive to the environment and instead regulated locally. At $M_{\text{star}} \gtrsim 10^{10} M_{\odot}$, the dispersion in SFRs becomes large. Part of the massive galaxy population starts to deviate to lower SFRs with respect to the main sequence by more than 1 dex. In our model, BHs rapidly grow in hosts with $M_{\text{star}} \gtrsim 10^{10} M_{\odot}$ (see figure 11). Therefore BH feedback can evacuate gas from galaxies and suppress star formation. Looking at the feedback energy, gas accretion at the Eddington limit onto a BH of $M_{\text{BH}} = 10^8 M_{\odot}$, generates $5.0 \times 10^{11} L_{\odot}$ in our model ($f_{\text{r}} f_{\text{e}} = 0.015$). That is much higher than the energy injection rate $\sim 0.8 \times 10^{10} L_{\odot}$ from SNe for a SFR $\sim 100 M_{\odot} \text{ yr}^{-1}$ which is typical for galaxies with $M_{\text{h}} \sim 10^{11} M_{\odot}$. Then, as the haloes grow, they can hold gas against feedback and form stars, resulting in SFRs near the main-sequence line.

If the angular resolution of observations is not high, the entire region of a halo can be observed. Therefore we also evaluate the total SFR and stellar mass of haloes in the PCR0 run. The most massive halo in the PCR0 shows a total SFR of $2679 M_{\odot} \text{ yr}^{-1}$ and $M_{\text{star}} = 2.5 \times 10^{12} M_{\odot}$, which corresponds to bright SMGs at $z \sim 3$ as seen in figure 12. Recent ALMA observations have revealed multiple components in bright SMGs detected with SCUBA and suggest that multiple dusty star-forming galaxies are hosted in massive haloes (Simpson et al. 2015). Our simulations suggest that multiple SMGs resolved by ALMA can be hosted in a common massive halo that is a very bright SMG identified by a single-dish submillimeter telescope, e.g., SCUBA-2, ASTE (e.g., Tamura et al. 2009).

In our simulations, even active star-forming galaxies are distributed within ~ 0.5 dex from the main-sequence line. On the other hand, some observed SMGs showed ~ 1 dex higher SFRs at a specific stellar mass ($\sim 10^{11} M_{\odot}$) than the main-sequence. Because of the limited numerical resolutions, we force the polytropic equation of state to ISM once the local density exceeds the threshold for star formation ($n_{\text{H}} \sim 0.1 \text{ cm}^{-3}$) to avoid the artificial fragmentation.

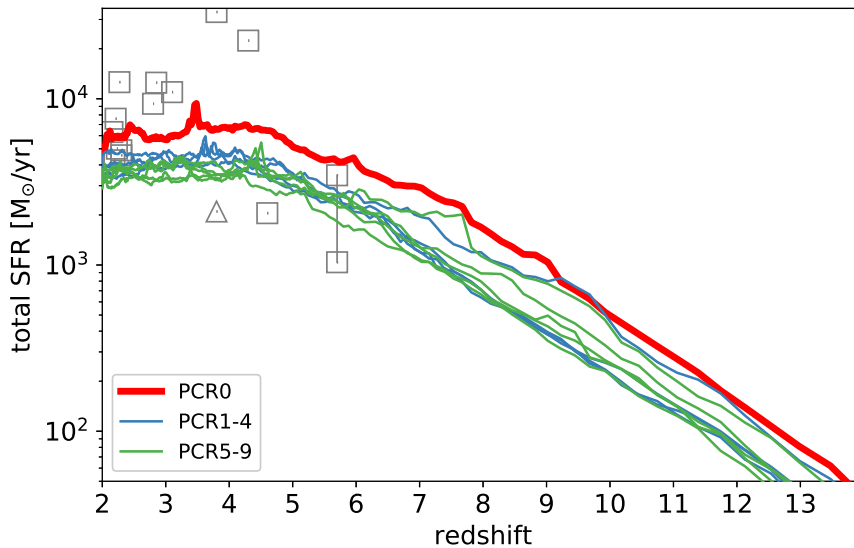


Figure 3. Total SFR within 10 cMpc from the centre of mass considering massive haloes with $M_h \geq 10^{12} M_\odot$ in each zoom-in region. Red thick solid line shows the PCR0 run. Blue and green lines represent PCR1-4 and PCR 5-9 runs. Open squares are the observed total SFRs of protocluster candidates by Lacaille et al. (2019), Mitsuhashi (2020), Clements et al. (2016), Harikane et al. (2019) and Kubo et al. (2019). The lower and upper values at $z = 5.7$ assume that the fraction of associated submillimeter galaxies is 0.3 and 1.0, respectively, accounting for redshift uncertainty (Harikane et al. 2019). The open triangle is the data without AGN contribution derived in Kubo et al. (2019).

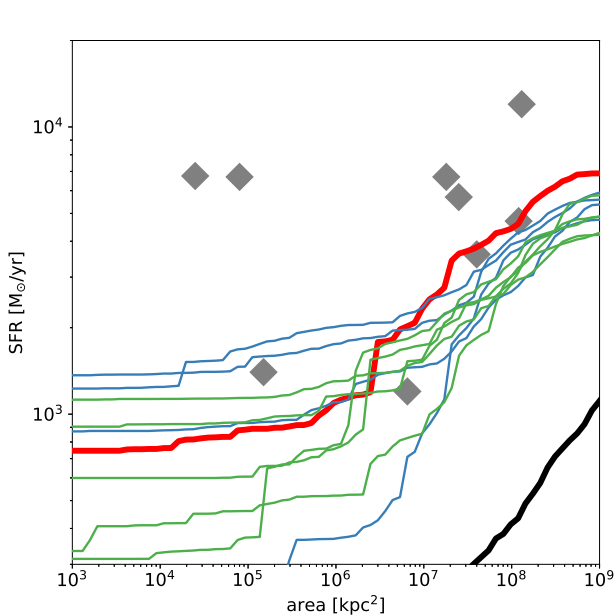


Figure 4. Cumulative SFR within a specific sky-area at $z = 3$. The meaning of the colored solid lines is the same as in Figure 3. The black solid line is the total SFR in the MF run. Gray diamonds are the observed total SFRs of protocluster candidates shown in figure 2 in Miller et al. (2018).

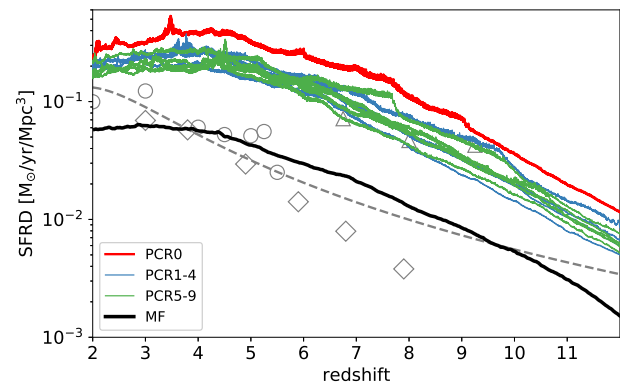


Figure 5. Cosmic star formation rate density. The meaning of the different lines is the same as in Figure 4. Open symbols show the observational data: diamonds from Bouwens et al. (2020), circles ALMA ALPINE survey (Khusanova et al. 2020; Gruppioni et al. 2020; Loiacono et al. 2020), triangles from Kistler et al. (2009). The black dashed line shows the extrapolated fitting function for UV-selected galaxies at $z \leq 10$ derived in Madau & Dickinson (2014).

While this model can keep a stable galactic disc and reproduce the observed galaxy sizes (Furlong et al. 2015), the violent disc instability may not be followed. Therefore, if a high sSFR is induced by a disc instability, we need to relax forcing particles onto the EOS via increasing the numerical resolution.

Figure 8 shows the stellar-to-halo mass ratios (SHMRs).

The SHMRs increase monotonically at $M_h \lesssim 10^{12.5} M_\odot$ and then decrease toward the massive end. The star formation in low-mass haloes is suppressed due to the SN feedback. Therefore, SHMRs of low-mass halos with $M_h \sim 10^{11} M_\odot$ can change with the parameter f_{th} by a factor of few (see also, Crain et al. 2015). Given that a weaker SN feedback model or $f_{\text{th}} = 1$ is used, the SFR and stellar mass of low-mass haloes increase significantly. As the halo mass increases, haloes can hold the gas against SN feedback and allow efficient star formation, resulting in the high SHMRs $\gtrsim 10^{-2}$ at $M_h \sim 10^{12} M_\odot$. In massive haloes with $M_h \gtrsim 10^{13} M_\odot$, the gas fraction of galaxies decreases, and SMBHs can provide additional strong feedback. Therefore, the SHMRs of massive galaxies in the PC regions become smaller SHMR $\lesssim 10^{-2}$.

The ratio of gas mass to total baryon mass (gas+stars) is presented in figure 9. The gas mass fraction (f_{gas}) monotonically decreases as the stellar mass increases. We find $f_{\text{gas}} \gtrsim 0.8$ at $M_{\text{star}} \sim 10^8 M_\odot$ and $f_{\text{gas}} \lesssim 0.4$ at $M_{\text{star}} \gtrsim 10^{11} M_\odot$. This implies that the gas in galaxies is consumed by star formation at a higher rate than the gas fueling. Also, in massive haloes, AGN feedback can contribute to expel the gas, and the cooling time of halo gas is long, suppressing the recovery of gas. Troncoso et al. (2014) estimated the gas content of galaxies at $3 \leq z \leq 5$, including the SSA22 region, by combining SFRs within specific radii and the Schmidt-Kennicutt relation. We estimate the gas fraction using the gas and stellar mass within $2 \times r_{0.5}$. Our results match the observations. Note that, however, the observations consider cold neutral gas alone. Our simulations cannot distinguish cold gas alone and include hot ionized gas due to resolution limitations, and the pressure floor using the polytropic equation of state with $\gamma = 4/3$ is used. Therefore our estimation of f_{gas} can be somewhat higher than if considering cold gas alone. We also estimate f_{gas} by using the total stellar and gas masses in haloes, i.e., within a virial radius. It shows the high values of $\gtrsim 0.8$, irrespective of the stellar mass as seen by the open circles and triangles. These discrepancies of f_{gas} between haloes and galaxies (star-forming regions) imply that most of the gas keeps being trapped in massive haloes even if they are pushed by the feedback. The cooling time of the halo gas can be estimated as

$$\begin{aligned} t_{\text{cool}} &= \frac{3kT}{2n_{\text{H}}^2 \Lambda(T)} \\ &= 3.3 \text{ Gyr} \left(\frac{T}{10^6 \text{ K}} \right) \left(\frac{n}{10^{-3} \text{ cm}^{-3}} \right) \left(\frac{\Lambda(T)}{10^{-23} \text{ erg s}^{-1} \text{ cm}^3} \right)^{-1} \end{aligned} \quad (15)$$

where $\Lambda(T)$ is the radiative cooling rate. If the temperature of the halo gas is close to the virial temperature, the cooling time of massive haloes with $M_h \gtrsim 10^{12} M_\odot$ is longer than the depletion time while on the main-sequence:

$$\begin{aligned} t_{\text{dep}} &\sim \frac{M_{\text{disc}}}{\text{SFR}} \\ &\sim 1.0 \text{ Gyr} \left(\frac{f_{\text{disc}}}{0.05} \right) \left(\frac{M_h}{10^{12} M_\odot} \right) \left(\frac{\text{SFR}}{250 M_\odot \text{ yr}^{-1}} \right)^{-1}, \end{aligned} \quad (16)$$

where f_{disc} is the mass ratio of gaseous disc to the halo mass. Once galaxy merger or disc instability occurs, the disc quickly loses angular momentum, resulting in gas flow to

the galactic center. In that case, SFRs are likely to be proportional to $C_* M_{\text{disc}}/t_{\text{dyn}}$, where C_* is the conversion efficiency from the inflow rate to SFR and t_{dyn} is the dynamical time of the galactic disk which can be evaluated as

$$\begin{aligned} t_{\text{dyn}} &\sim \frac{\lambda R_{\text{vir}}}{V_\phi} \\ &\sim 1.5 \times 10^{-2} \text{ Gyr} \left(\frac{\lambda}{0.05} \right) \left(\frac{M_h}{10^{12} M_\odot} \right) \\ &\quad \times \left(\frac{1+z}{4} \right)^{-1} \left(\frac{V_\phi}{250 \text{ km s}^{-1}} \right)^{-1}, \end{aligned} \quad (17)$$

where λ is the halo spin parameter and V_ϕ is the rotation velocity of the galactic disc. The consumption time scale of the gas is estimated as $\sim t_{\text{dyn}}/C_*$, and it becomes shorter than t_{dep} if $C_* > 1.5 \times 10^{-2}$. Thus, in the case of massive haloes, the cooling time scale can be longer than the time scale for consumption by star formation. Therefore, once the gas in the galactic disc is expelled into the halo via stellar or AGN feedback, the halo gas is likely to be hampered to accrete onto the star-forming regions due to the thermal pressure support if the radiative cooling is inefficient. This can induce the large discrepancy of f_{gas} seen between galaxies and haloes at $M_{\text{star}} \gtrsim 10^{10} M_\odot$.

On the other hand, some massive galaxies show high gas fraction with $f_{\text{gas}} \gtrsim 0.6$. As shown in Figure 1, massive haloes in the PCs form at the crossing of large-scale filaments. Therefore, the IGM filaments can feed massive galaxies with gas efficiently, leading to the formation of gas-rich massive galaxies. We will investigate the detailed motion of inflow and outflow of gas from massive haloes in future work.

Figure 10 presents gas phase metallicities. We measure the metallicity by using gas particles within $2 \times r_{0.5}$. As star formation proceeds, metals ejected from SNe are accumulated in galaxies. Therefore, the metallicity increases with the stellar mass monotonically. In low-mass haloes, a part of the metal-enriched gas can be expelled due to the galactic winds which results in a steep mass dependency of the metallicity. The metallicity reaches $\sim 0.5 \times$ solar abundance at $M_{\text{star}} \sim 10^{10} M_\odot$. At $M_{\text{star}} > 10^{10} M_\odot$, the metallicity becomes almost constant within $Z \sim 0.5 - 1 Z_\odot$. This trend is similar to reported observed relations (Maiolino et al. 2008; Mannucci et al. 2009; Onodera et al. 2016). Note that, however, some massive galaxies show somewhat lower metallicities. These galaxies are gas-rich as shown in Figure 9, which indicates that they are fueled by low-metallicity gas, likely from IGM filaments.

The metallicities of galaxies with $M_{\text{star}} \lesssim 10^9 M_\odot$ are somewhat higher than the observations. This is likely due to the arbitrary regions of measuring the metallicity in the simulations. For example, Shimizu et al. (2014) took into account the metallicities weighted by the local ionizing photon emissivities. If we consider wider regions, the metallicity at specific stellar-mass decreases because the gas metallicity becomes lower as the distance from the galactic center increases. As a reference, we also estimate the metallicity by using all gas particles in a halo. In that case, the metallicity becomes lower than the case using $2 \times r_{0.5}$ by a factor of 3-5. The metal distribution sensitively depends on the feedback model. We will study the relation between the metal distribution and the feedback models in future work.

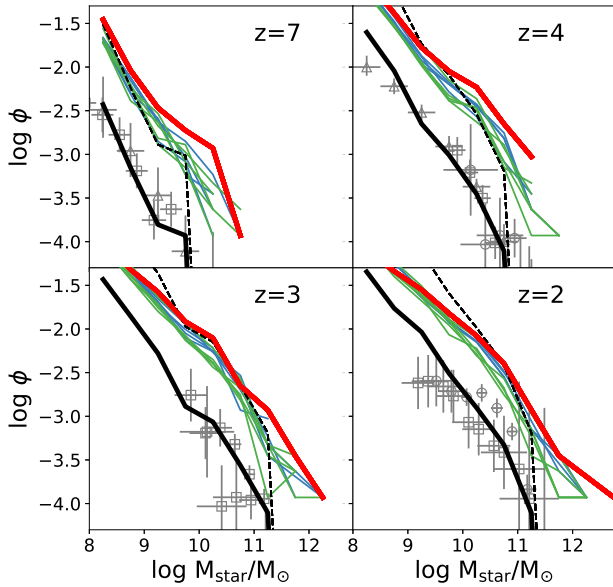


Figure 6. Stellar mass functions of MF and PCR runs at $z = 7, 4, 3$ and 2 . Line types are the same as in Figure 4. Black dashed line are the MF mass function scaled by a factor of 2.5. Open symbols show the observed stellar mass functions: $z=7$ (open squares: Bouwens et al. 2011), (open triangles: Song et al. 2016); $z=4$ (open circles: Marchesini et al. 2010), (open squares: Lee et al. 2012), (open triangles: Song et al. 2016); $z=3$ (open squares: Marchesini et al. 2010); $z=2$ (open squares: Mortlock et al. 2011), (open circles: Marchesini et al. 2010).

In addition, this might suggest that the observed SEDs with metal lines reflect gas at $> 2 \times r_{0.5}$. Future missions with PFS on the Subaru telescope will investigate the radial distribution of metals using metal absorption lines in SEDs of background galaxies. The comparison of our simulations with future observation will allow understanding the origin of the discrepancies reported above.

3.2 Massive black holes in PC regions

Massive BHs at galactic centres are ubiquitous in the local Universe (Kormendy & Ho 2013). The black hole mass is tightly correlated with the bulge mass of galaxies via $M_{\text{BH}} \sim 2 \times 10^{-3} M_{\text{star}}$ (e.g., Marconi & Hunt 2003). While this correlation has been well established at low redshifts, it is still unclear how it looks at high redshift due to the limited number of observed massive black holes. Figure 11 shows the BH mass as a function of stellar mass. BHs grow slowly at $M_{\text{star}} \lesssim 10^{10} M_{\odot}$ and then do rapidly as the galaxies become more massive. As suggested by Dubois et al. (2016), SN feedback evacuates gas around a BH and suppresses the gas accretion onto it. Once the halo mass exceeds $\sim 10^{11-12} M_{\odot}$, the deep gravitational potential well associated with the halo keeps the gas confined at the galactic center against SN feedback. Therefore, the gas disc around the BH can become massive enough and allow gas inflow to the galactic centre via clump formation and bar instability

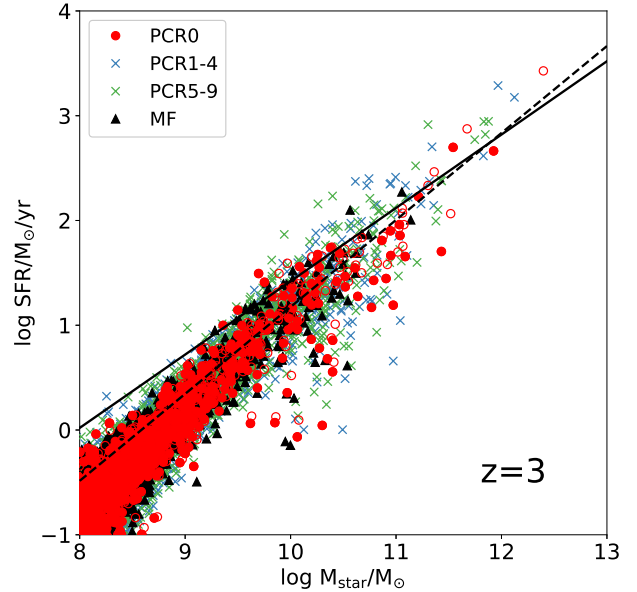


Figure 7. Star formation rates of galaxies as a function of stellar mass. Different symbols represent each run: PC0 (filled red circles), PC1-4 (blue crosses), PC5-9 (green crosses), and MF (filled black triangles). The stellar mass and SFR are estimated within $2 \times r_{0.5}$ where $r_{0.5}$ is the half stellar mass radius of a most massive galaxy in a halo. Open red circles show the case using total stellar mass and SFR in a halo. Black dashed and solid lines show the relations of observed galaxies at $z = 2.3 - 2.9$ and $z = 2.9 - 3.8$ derived in Pearson et al. (2018).

(Shlosman et al. 1989; Shlosman & Noguchi 1993). During this phase, the BHs grow at the Eddington limit and the BH mass increase as $M_{\text{BH}} \propto \exp(t/t_{\text{Sal}})$, where t_{Sal} is Salpeter time scale, $t_{\text{Sal}} = \frac{f_{\text{Edd}} \sigma_{\text{T}} c}{4\pi G m_{\text{p}}} \sim 45$ Myr. The energy injection rate is estimated as

$$\dot{E}_{\text{BH,feed}} = 5.0 \times 10^{11} L_{\odot} \left(\frac{f_{\text{Edd}}}{1.0} \right) \left(\frac{f_e}{0.15} \right) \left(\frac{M_{\text{BH}}}{10^8 M_{\odot}} \right). \quad (18)$$

Given than the gas accretion continues for a Salpeter time and a part of thermal energy is converted into kinetic one, the total kinetic energy is

$$E_{\text{kin}} \sim 2.7 \times 10^{59} \text{ erg} \left(\frac{f_{\text{conv}}}{0.1} \right) \left(\frac{\Delta t}{45 \text{ Myr}} \right) \times \left(\frac{f_{\text{Edd}}}{1.0} \right) \left(\frac{f_e}{0.15} \right) \left(\frac{M_{\text{BH}}}{10^8 M_{\odot}} \right), \quad (19)$$

where f_{conv} is the conversion factor from thermal energy to the kinetic and Δt as the accretion time scale of gas. On the other hand, the gravitational binding energy of the gas in a halo with $M_{\text{h}} \sim 10^{13} M_{\odot}$ is estimated by

$$E_{\text{grav}} \sim 1.1 \times 10^{59} \text{ erg} \left(\frac{M_{\text{h}}}{10^{13} M_{\odot}} \right)^2 \left(\frac{\xi_{\text{M}}}{0.1} \right)^2 \left(\frac{\xi_{\text{gas}}}{0.1} \right) \left(\frac{1+z}{4} \right), \quad (20)$$

where ξ_{M} is the fraction of total matter mass within the star-forming region (e.g., $\lambda \times R_{\text{vir}}$ where λ is the halo spin parameter (Mo & White 2002)) to the total halo mass and

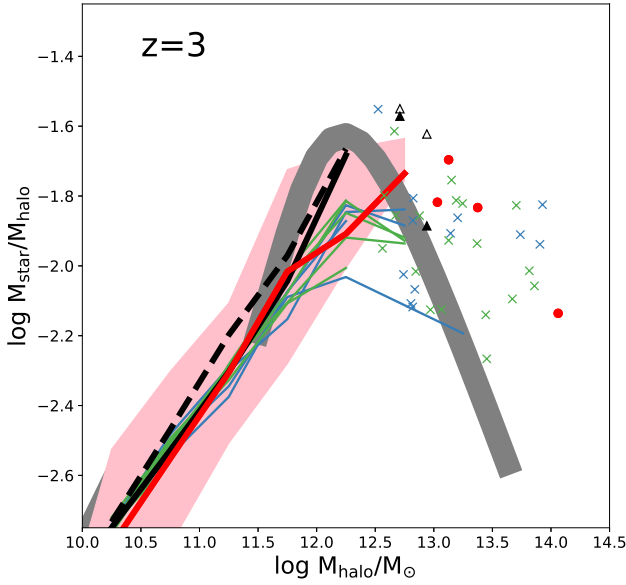


Figure 8. Stellar to halo mass ratio as a function of halo mass. The bin size is $\Delta \log M_h/M_\odot = 0.25$. Lines represent the median values in each bin. Line types are the same as in Figure 4. If the number of galaxies in a bin is smaller than five, the values of the galaxies are shown as symbols. Different symbols show different runs, same as in figure 7. The stellar mass is estimated within $2 \times r_{0.5}$. The pink and gray shades show the quartiles (25 - 75 percent) in each bin in PC0 and MF runs. Black dashed line and open triangles are based on the total stellar mass in haloes in MF run. The gray thick curve is taken from Behroozi et al. (2013).

ξ_{gas} is the fraction of total gas mass to the total matter mass within the star-forming region. Therefore BH feedback can evacuate the gas from the star-forming region and suppress star formation although it does not continue for a long time due to the self-regulation of BH growth. Then, as the halo grows, galaxies can confine the gas and form stars (see also Figure 7), while the growth of BHs is not so efficient due to the high-relative gas motion and low-gas density. Some BHs reach $\sim 10^9 M_\odot$ as their host galaxy mass increases. During this phase, BH growth stalls due to the powerful quasar and radio mode feedback while the stellar mass increases, ultimately leading to massive galaxies with $M_{\text{star}} \gtrsim 10^{11} M_\odot$ having SMBHs with masses as expected from the local relation.

3.3 Infrared properties

In order to investigate the observational signatures of the galaxies in the PC regions, we carry out radiative transfer simulations in post-processing. Figure 12 presents IR luminosities (L_{IR}), fluxes at 1.1 mm in the observed frame ($S_{1.1\text{mm}}$) and escape fractions of UV and Lyman continuum photons. Here we estimate the radiative properties of the 300 most massive haloes in the PCR0 run. L_{IR} and $S_{1.1\text{mm}}$ increase with stellar mass. The most massive halo has $L_{\text{IR}} = 6.0 \times 10^{13} L_\odot$ and $S_{1.1\text{mm}} = 29.4 \text{ mJy}$.

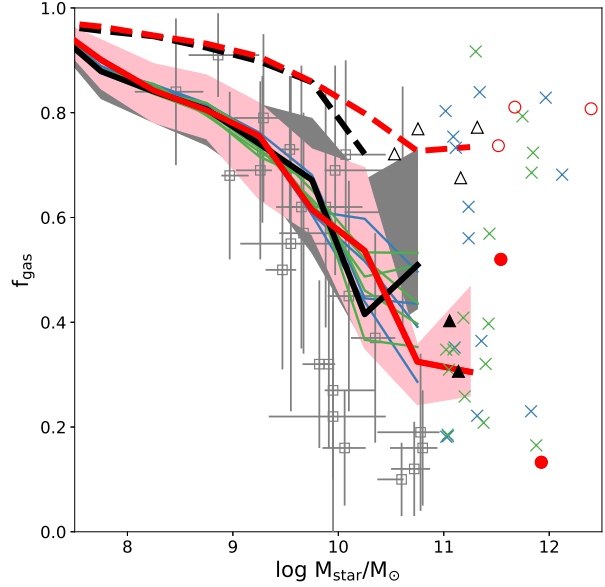


Figure 9. Gas mass to total baryon mass (gas + stars) fraction f_{gas} as a function of stellar mass. The pink and gray shades show the quartiles (25 - 75 percent) in each bin in PC0 and MF runs. Different lines and symbols represent different runs, same as in figures 8. The red thick dashed line and open circles show the case using all gas and stars in haloes of PCR0. The black thick dashed line and open triangles are the cases using all gas and stars in haloes of the MF run. Gray open squares with error bars show the observed gas fractions in Troncoso et al. (2014).

As the galaxy mass increases, dusty gas accumulates in star-forming regions and absorbs UV radiation efficiently. Therefore, f_{esc} decreases as the stellar mass increases. At $M_{\text{star}} \gtrsim 10^{11} M_\odot$, f_{esc} become smaller than ~ 0.2 . Recently, Wang et al. (2019) indicated that the fraction of dust-obscured galaxies becomes larger than UV bright galaxies (LBGs) at $M_{\text{star}} \gtrsim 10^{10.5} M_\odot$. Our results are consistent with their results. Due to the mass dependence of f_{esc} , L_{IR} and $S_{1.1\text{mm}}$ increase more steeply than the relation between SFR and M_{star} in figure 7. Umehata et al. (2020) estimated the stellar mass and submillimeter flux of an SMG at $z = 4.0$. In addition, Dudzevičiūtė et al. (2020) successfully derived the physical properties of 707 SMGs at $z = 1.8 - 3.4$. Our modeled galaxies with similar stellar masses match those observations well. Yajima et al. (2015b) also showed the formation of dusty starburst galaxies at $z \gtrsim 6$. In the previous study, we showed results for a massive galaxy with $M_{\text{star}} = 8.4 \times 10^{10} M_\odot$ and $L_{\text{IR}} = 3.7 \times 10^{12} L_\odot$ at $z = 6.3$, which are similar to our current results. In this paper, we have expanded the mass and redshift range, as well as added new sub-grid models.

At $M_{\text{star}} \sim 10^{10} - 10^{11} M_\odot$, there is a large dispersion in f_{esc} . Some galaxies have very high f_{esc} of > 0.5 likely due to the galactic outflows. Therefore these galaxies are faint at sub-millimeter wavelengths with $S_{1.1\text{mm}} \lesssim 10^{-2} \text{ mJy}$. This suggests that the population of galaxies in this mass range is not homologous. Arata et al. (2019) showed that

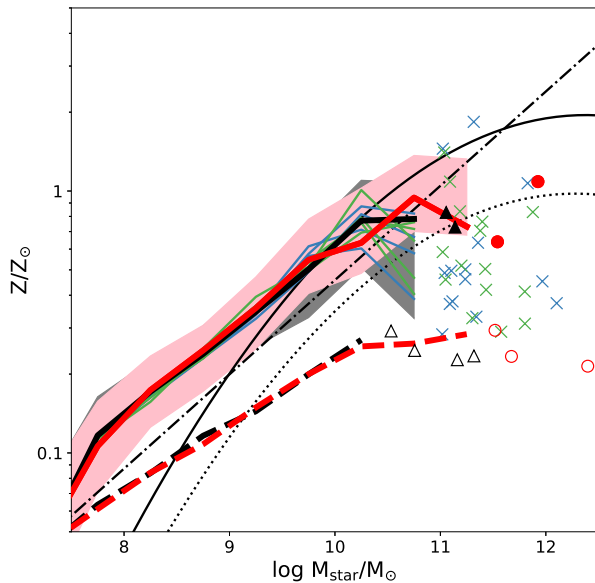


Figure 10. Gas metallicity as a function of stellar mass. Each line and symbol represent each run as in figure 9. The metallicity and stellar mass are estimated within $2 \times r_{0.5}$ of the most massive member galaxies. The pink and gray shades show the quartiles (25 - 75 percent) in each bin in PC0 and MF runs. Black solid, dotted, dot-dashed lines represent the relations of observed galaxies derived in Maiolino et al. (2008), Mannucci et al. (2009), and Onodera et al. (2016).

SN feedback induces galactic outflows and quenching of star formation and the radiative properties rapidly changed due to this (see also, Yajima et al. 2017a). We will investigate the radiative properties and the origin of the observed diversity by using a larger galaxy sample in a subsequent paper.

Note, in the current simulations the multi-phase ISM can not be resolved well due to the limited resolution. Therefore, ART² assumes a sub-grid model consisting of a two-phase ISM with cold gas clumps in a warm medium. In this case, the escape fraction can differ from the single-phase ISM model because some photons travel without interaction with the cold gas clump (Yajima et al. 2015b). We will investigate the impacts of the ISM model on the radiative properties in future. However, since f_{esc} of massive galaxies is lower than ~ 0.2 , their submillimeter fluxes do not change significantly even if f_{esc} decreases furthermore.

3.4 BCG runs

We study the time evolution of the most massive haloes in the BCG runs. Here, we evaluate total quantities in a halo, e.g., SFR refers to the total SFR in a halo. Figure 13 shows the star formation histories, stellar mass, and halo mass growth histories. The halo masses of the BCGs exceed $\sim 10^{12} M_{\odot}$ even at $z \sim 7$ and reach $M_{\text{h}} \sim 1 - 3 \times 10^{13} M_{\odot}$ at $z \sim 4$. All BCGs host galaxies with $M_{\text{star}} \gtrsim 10^{11} M_{\odot}$ at $z \lesssim 6$.

The SFR of BCG0 increases from $z \sim 10$ to ~ 7 sig-

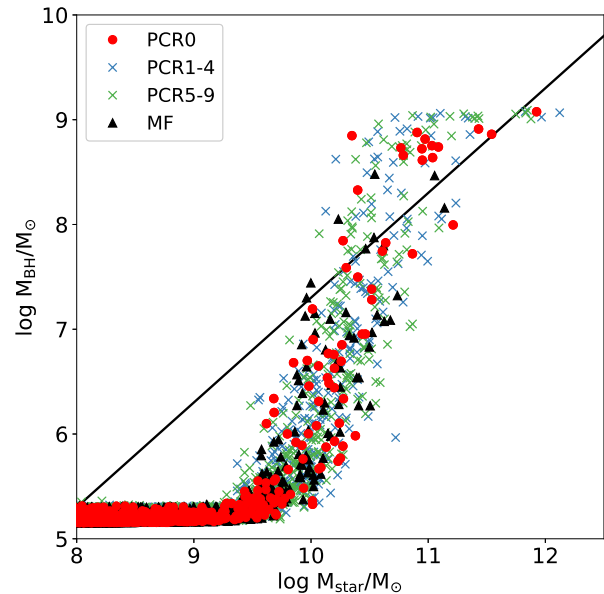


Figure 11. Masses of the most massive black holes in each galaxy as a function of stellar mass $z = 3$. The black solid line represent the observed relation in local galaxies, i.e., $M_{\text{BH}} = 2.0 \times 10^{-3} M_{\text{star}}$ (Marconi & Hunt 2003).

nificantly. This is because the halo can keep confining the gas against SN feedback as the halo mass becomes close to $M_{\text{h}} \sim 10^{12} M_{\odot}$ (see also figure 8). The SFR stays at $\sim 100 - 300 M_{\odot} \text{ yr}^{-1}$ at $z \sim 5 - 7$ while the halo grows slowly. At $z \lesssim 5$, the halo mass of BCG0 increases rapidly, resulting in a starburst with $\text{SFR} \gtrsim 1000 M_{\odot} \text{ yr}^{-1}$. Most BCGs have high SFRs with $\gtrsim 100 M_{\odot} \text{ yr}^{-1}$ even at $z = 6 - 8$, which is similar to observed dusty starburst galaxies (e.g., Walter et al. 2018). This suggests that observed dusty starburst galaxies form in protoclusters. BCG7 has the highest value of SFR at $z > 6$, which is $\text{SFR} = 1254 M_{\odot} \text{ yr}^{-1}$ at $z = 6.4$. This is similar to the bright SMG at $z = 6.3$, HFLS3 (Riechers et al. 2013; Cooray et al. 2014).

Recent observations indicated that passive galaxies form after the starburst phase (Glazebrook et al. 2017; Mawatari et al. 2020). However, all BCGs in our simulations keep high SFRs at $z \lesssim 6$. In our simulations, even if SN or BH feedback suppresses star formation for a while, dark matter and gas keep accreting on the haloes and avoid quenching of star formation for a long time ($\gtrsim 1 \text{ Gyr}$). Our result thus suggests that it may require a rare situation where the growth rate of a halo is quite small for a long time. We will investigate such setups using a larger sample in future work.

In most BCGs, SMBHs with $M_{\text{BH}} > 10^8 M_{\odot}$ form at $z \lesssim 6$. Therefore, BH feedback can play a role in regulating star formation and shaping the gas structure. Figure 14 shows the star formation histories, the growth histories of stellar and BH mass of BCG0, BCG0noAGN, and BCG0spEdd. Given that the upper limit of the Eddington ratio is set to 5 (BCG0spEdd), the BH mass rapidly increase from $\sim 10^5$ to $\sim 10^8 M_{\odot}$ at $z = 8 - 10$. Then it achieves $10^9 M_{\odot}$ at

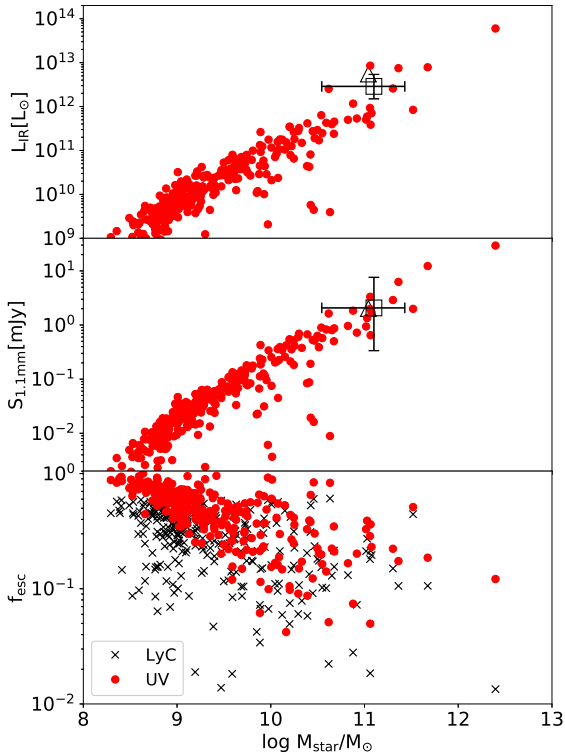


Figure 12. Results of radiative transfer simulations of the 300 most massive galaxies in PCR0 at $z = 3$. Top panel: Bolometric infrared luminosities as a function of total stellar mass in haloes. Middle panel: Submillimeter fluxes at 1.1 mm in the observed frame. Open triangles represent a submillimeter galaxy at $z = 4$ (Umehata et al. 2020). Open squares with error bars show 707 submillimeter galaxies at $z = 1.8 - 3.4$ (Dudzevičiūtė et al. 2020). Lower panel: Escape fractions of UV (filled circles) and Lyman continuum (crosses) photons.

$z = 6.5$ after the stalling phase. Due to the self-regulation via the quasar and radio mode feedback processes, the growth of the BH becomes slow. Finally, the mass of the BH in BCG0spEdd is $1.3 \times 10^9 M_\odot$ at $z=4.0$. On the other hand, BCG0 hosts the BH with $M_{\text{BH}} = 6.7 \times 10^7 M_\odot$ even at $z = 6.0$. The growth rate of the BH mass becomes small at $z = 4.8 - 6.2$ when the halo growth is slow. At $z < 5$, the BH mass increases via the merger of BHs and achieves $M_{\text{BH}} = 3.4 \times 10^8 M_\odot$. Therefore, we suggest that the growth history of a BH depends on the upper limit of the accretion rate. The upper limit is likely to be determined by unresolved small-scale structure, i.e., the gas distribution, angular momentum, and anisotropy of the radiation from an accretion disk. If the gas structure and the flux from an accretion disk are isotropic, the accretion rate should not exceed the Eddington limit (but see, Inayoshi et al. 2016). On the other hand, given that the anisotropies of gas and radiation, the accretion rate can be estimated by the Bondi-Hoyle-Littleton model and be larger than the Eddington limit (e.g., Sugimura et al. 2017).

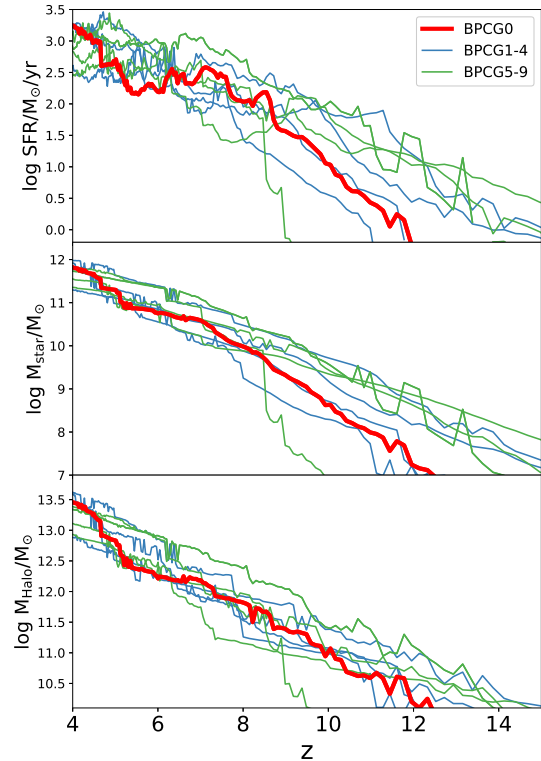


Figure 13. Redshift evolution of SFR, stellar mass and halo mass of BCG runs.

BH feedback suppresses the star formation as shown in the upper panel. In the case of BCG0, the SFR becomes smaller than BCGnoAGN by a factor of 1-3 at $z \lesssim 6$. At $z > 6$, the difference of the SFRs is quite small although the BH grows almost at the Eddington limit at $z \sim 6 - 10$. This suggests that the injected thermal energy is lost efficiently by radiative cooling before it induces a large-scale galactic outflow. In the case of BCG0spEdd, the reduction rate of the SFR is much larger, it is lower than BCGnoAGN by an order of unity at $z \lesssim 7$. As a result, M_{star} of BCG0spEdd is lower than BCGnoAGN by a factor of 3.5 at $z = 4.0$, while there is no large difference between BCG0 and BCGnoAGN.

3.5 First runs

Metal enrichment of the universe proceeds inhomogeneously (Wise et al. 2012; Pallottini et al. 2014; Hicks et al. 2020). The overdensity regions are likely to be metal-enriched earlier than the mean-density field. Therefore, the transition from Pop III to Pop II stars occurs earlier. Here, we investigate the transition of the stellar population.

Figure 15 presents the total star formation rates of Pop III and Pop II stars in the zoom-in regions. At $z \sim 30$, Pop III stars form gradually with a rate of $\sim 10^{-2} M_\odot \text{ yr}^{-1}$. Due to the SNe of Pop III stars, the gas is metal-enriched, and Pop II stars start to form at $z \sim 25$. The total SFRs of

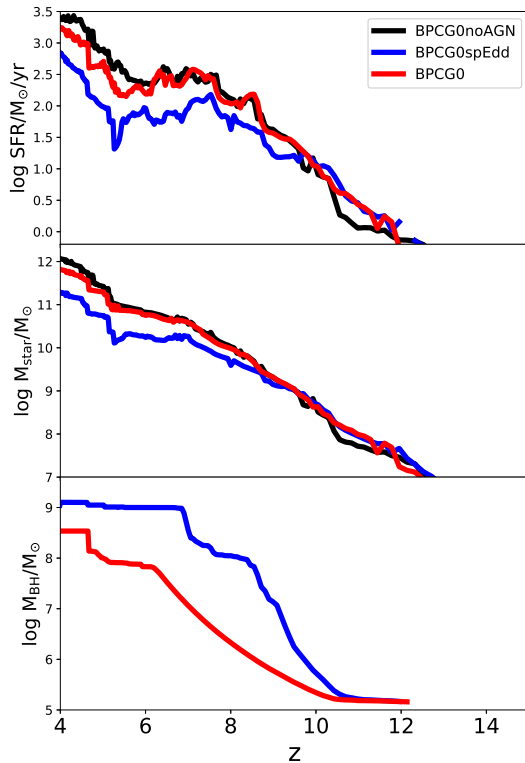


Figure 14. Same as figure 13, but comparing BCG0, BCG0noAGN and BCG0spEdd.

Pop III stars keep increasing up to $z \sim 15$. Then it decreases gradually at $z \sim 10-15$. On the other hand, the SFR of Pop II stars increases with time monotonically. The SFR of Pop II stars exceeds that of Pop III stars at $z \sim 20$. It is earlier than the mean density field, $z \sim 15$, as shown in Johnson et al. (2013). Also, as the SFR increases, mini-haloes with pristine gas are irradiated by strong LW radiation from star-forming galaxies, resulting in the suppression of the formation of Pop III stars. At $z \sim 10$, the SFR of Pop II stars become ~ 100 times higher than that of Pop III stars.

Because of the rapid halo growth in the overdensity regions, the most massive haloes form stars actively with $\text{SFR} \gtrsim 18 M_{\odot} \text{ yr}^{-1}$ even at $z \gtrsim 10$. These galaxies can emit strong Ly α , H α lines, and metal lines. Therefore they can be prime targets in future observations with ALMA, JWST, and other 30-m class telescopes (e.g., E-ELT, TMT, GMT).

Also, wide-field near-infrared imaging surveys would be key to finding such rare overdense regions. Future missions with e.g. Euclid and the Roman space telescopes will be expected to search for such regions.

4 DISCUSSION & SUMMARY

In this paper, we introduce a new simulation project FOREVER22: FORmation and EVolution of Extremely-

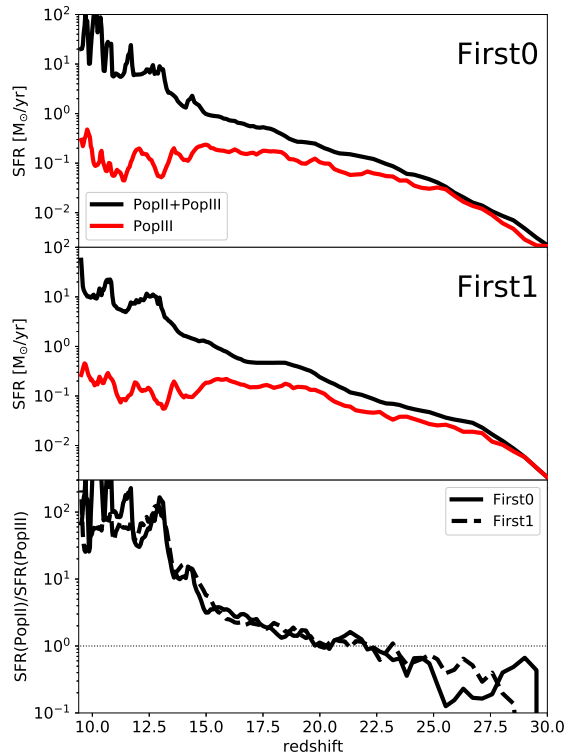


Figure 15. Star formation rate histories of First0 and First1 runs. Bottom panel shows the ratio of star formation rates of Population II to Population III stars.

overdense Regions motivated by SSA22. In this project, we study galaxy evolution in protocluster (PC) regions using cosmological hydrodynamics simulations with zoom-in initial conditions. FOREVER22 consists of three types of runs with the different resolutions and zoom-in volumes. Using these simulations, we study the statistical natures of galaxies in PCs, gas dynamics of individual galaxies, and feedback processes. We select 10 protocluster regions from a cosmological box of size of $L = 714 \text{ cMpc}$.

The main conclusions of this paper are the following points:

1) In the PC regions at $z = 3$, the most massive halo reaches a halo mass of $M_h = 1.2 \times 10^{14} M_{\odot}$ and hosts a supermassive black hole (SMBH) with $M_{\text{BH}} = 1.2 \times 10^9 M_{\odot}$. BHs grow rapidly as the host stellar mass exceeds $\sim 10^{10} M_{\odot}$. Then, the growth of supermassive BHs is suppressed due to their feedback, while the host stellar mass continues to increase. BH masses in massive haloes follow the observed local BH mass and bulge mass relation (e.g., Marconi & Hunt 2003).

2) More than five starburst galaxies with $\text{SFR} \gtrsim 100 M_{\odot} \text{ yr}^{-1}$ form in the massive haloes with $M_h \gtrsim 10^{13} M_{\odot}$ at the core of a PC region at $z = 3$. The most massive halo

has a cumulative SFR of $2679 M_{\odot} \text{ yr}^{-1}$. These massive active galaxies are dust-obscured, resulting in the bright submillimeter flux densities of $\gtrsim 1 \text{ mJy}$ at 1.1 mm. Yajima et al. (2015b) investigated the formation of dusty massive galaxies with $M_{\text{star}} \sim 8.4 \times 10^{10} M_{\odot}$ at $z = 6.3$. The infrared luminosities of our modelled massive galaxies are quantitatively similar to the previous study. In this work, we have expanded the ranges of redshift and halo mass with new sub-grid models including massive BHs.

3) The metal enrichment proceeds efficiently via type-II supernovae in the early Universe and the dominant stellar population changes from Pop III to Pop II at $z \sim 20$. In the metal-enriched PC cores, the first galaxies with SFRs $\gtrsim 18 M_{\odot} \text{ yr}^{-1}$ form at $z \sim 10$.

Thus, we suggest that PCs can be the formation sites of bright submillimeter galaxies and SMBHs at $z \sim 3$. The clustering of dusty galaxies are similar to the one in observed protoclusters, e.g., SSA22 region. In addition, the bright first galaxies at $z \gtrsim 10$ can be prime targets for future observations by *James Webb Space Telescope*.

In this paper, we mainly present an overview of the properties of galaxies in the PCs at $z = 3$. Recently, Bouwens et al. (2020) showed the contribution of bright SMGs to the cosmic SFR density over a wide redshift range (see also, Wang et al. 2019). They indicated that the contribution becomes much smaller than that of UV-selected galaxies at $z \gtrsim 4$. This is closely related to the redshift evolution of the star formation activity and dust distribution in massive haloes in PCs. In addition, the cosmic reionization proceeds inhomogeneously, and the over-dense regions can form ionized bubbles earlier in in-side out fashion (e.g. Iliev et al. 2012). Therefore, the PCs can be the first triggers of reionization, although the escape probability of ionizing photons decreases as the halo mass increases (e.g., Yajima et al. 2011, 2014; Wise et al. 2014; Paardekooper et al. 2015; Trebitsch et al. 2017; Ma et al. 2020). We will investigate other statistical properties over a wide redshift range and the origin of the observed diversity of high-redshift galaxies in a future papers.

In the PCs regions, the growth rate of halo mass is much faster than in the mean-density field, resulting in the formation of massive haloes with $\gtrsim 10^{13} M_{\odot}$ at $z \sim 3$. However, at a specific stellar or halo mass, the star formation, the gas fraction, and the metallicity of the PCs are similar to those of the mean density field, although some galaxies in the PCs have lower SFRs and have more massive BHs. Therefore, we suggest that the external environmental effects (e.g., galaxy merger, tidal force) on the properties such as stellar mass and star formation rate are not significant.

The massive galaxies in the PC regions show normal star formation activity, lying along the observed star formation main-sequence. In particular, the dispersion of sSFRs of massive galaxies is not significant. On the other hand, recent observations indicated that some massive galaxies enter the passive phase even at $z \gtrsim 2$ (Glazebrook et al. 2017). In the current simulations, although stellar and AGN feedback evacuate gas from star-forming regions, the circum-galactic medium or IGM filaments feed galaxies with gas, resulting

in continuous star formation. Therefore, the early quenching of star formation is likely to depend on the feedback model. Stronger feedback can delay the refueling time-scale and may induce the formation of the passive galaxies. Due to the limited resolution, AGN feedback is modeled via a sub-grid model with free parameters, e.g., the thermal coupling factor. In addition, Yajima et al. (2017a) showed that the higher amplitude factor in the star formation model induced large fluctuations in star formation history. We will investigate the quenching mechanism of massive galaxies at high-redshifts by changing these conditions in our future work.

ACKNOWLEDGMENTS

We are grateful to Masayuki Umemura, Ken Ohsuga and Kazuyuki Sugimura for valuable discussion and comments. The numerical simulations were performed on the computer cluster, XC50 in NAOJ, and Trinity at Center for Computational Sciences in University of Tsukuba. This work is supported in part by MEXT/JSPS KAKENHI Grant Number 17H04827, 20H04724 (HY), 17H01111, 19H05810, 20H00180 (KN), 17H0481, 17KK0098, 19H00697, 20H01953 (YM), 20K14530 (MK) and NAOJ ALMA Scientific Research Grant Numbers 2019-11A.

DATA AVAILABILITY

The data underlying this article will be shared on reasonable request to the corresponding author.

REFERENCES

- Agarwal B., Khochfar S., 2015, MNRAS, 446, 160
- Agarwal B., Smith B., Glover S., Natarajan P., Khochfar S., 2016, MNRAS, 459, 4209
- Arata S., Yajima H., Nagamine K., Abe M., Khochfar S., 2020, MNRAS, 498, 5541
- Arata S., Yajima H., Nagamine K., Li Y., Khochfar S., 2019, MNRAS, 488, 2629
- Barnes D. J. et al., 2017, MNRAS, 471, 1088
- Behroozi P. S., Wechsler R. H., Conroy C., 2013, ApJ, 770, 57
- Benson A. J., Hoyle F., Torres F., Vogeley M. S., 2003, MNRAS, 340, 160
- Bondi H., Hoyle F., 1944, MNRAS, 104, 273
- Bouwens R. J. et al., 2020, ApJ, 902, 112
- Bouwens R. J. et al., 2011, ApJ, 737, 90
- Bouwens R. J. et al., 2015, ApJ, 803, 34
- Bromm V., Loeb A., 2003, ApJ, 596, 34
- Capak P. L. et al., 2015, Nature, 522, 455
- Casey C. M., Cooray A., Capak P., Fu H., Kovac K., Lilly S., Sanders D. B., Scoville N. Z., Treister E., 2015, ApJ, 808, L33
- Casey C. M., Narayanan D., Cooray A., 2014, Phys. Rep., 541, 45
- Chapman S. C., Blain A. W., Smail I., Ivison R. J., 2005, ApJ, 622, 772
- Chiang Y.-K., Overzier R. A., Gebhardt K., Henriques B., 2017, ApJ, 844, L23

- Cioffi D. F., McKee C. F., Bertschinger E., 1988, *ApJ*, 334, 252
- Clements D. L. et al., 2016, *MNRAS*, 461, 1719
- Cooray A. et al., 2014, *ApJ*, 790, 40
- Crain R. A. et al., 2015, *MNRAS*, 450, 1937
- Cui W. et al., 2018, *MNRAS*, 480, 2898
- Cullen F., McLure R. J., Khochfar S., Dunlop J. S., Dalla Vecchia C., 2017, *ArXiv e-prints*
- Daddi E. et al., 2005, *ApJ*, 626, 680
- Dalla Vecchia C., Schaye J., 2012, *MNRAS*, 426, 140
- Di Matteo T., Croft R. A. C., Feng Y., Waters D., Wilkins S., 2017, *MNRAS*, 467, 4243
- Draine B. T., Bertoldi F., 1996, *ApJ*, 468, 269
- Draine B. T., et al., 2007, *ApJ*, 663, 866
- Dubois Y., Devriendt J., Slyz A., Teyssier R., 2012, *MNRAS*, 420, 2662
- Dubois Y., Peirani S., Pichon C., Devriendt J., Gavazzi R., Welker C., Volonteri M., 2016, *MNRAS*, 463, 3948
- Dudzėvičiūtė U. et al., 2020, *MNRAS*, 494, 3828
- Elliott J., Khochfar S., Greiner J., Dalla Vecchia C., 2015, *MNRAS*, 446, 4239
- Esdaile J. et al., 2020, *arXiv e-prints*, [arXiv:2010.09738](https://arxiv.org/abs/2010.09738)
- Faucher-Giguère C., Lidz A., Zaldarriaga M., Hernquist L., 2009, *ApJ*, 703, 1416
- Ferland G. J., 2000, in *Revista Mexicana de Astronomia y Astrofisica Conference Series*, Vol. 9, *Revista Mexicana de Astronomia y Astrofisica Conference Series*, Arthur S. J., Brickhouse N. S., Franco J., eds., pp. 153–157
- Finkelstein S. L. et al., 2013, *Nature*, 502, 524
- Furlong M. et al., 2015, *MNRAS*, 450, 4486
- Glazebrook K. et al., 2017, *Nature*, 544, 71
- Glover S. C. O., Brand P. W. J. L., 2001, *MNRAS*, 321, 385
- Gruppioni C. et al., 2020, *arXiv e-prints*, [arXiv:2006.04974](https://arxiv.org/abs/2006.04974)
- Haardt F., Madau P., 1996, *ApJ*, 461, 20
- Haardt F., Madau P., 2001, in *Clusters of Galaxies and the High Redshift Universe Observed in X-rays*, Neumann D. M., Tran J. T. V., eds.
- Harikane Y. et al., 2019, *ApJ*, 883, 142
- Hashimoto T. et al., 2018, *Nature*, 557, 392
- Hatsukade B. et al., 2018, *PASJ*, 70, 105
- Hayashi M., Kodama T., Tanaka I., Shimakawa R., Koyama Y., Tadaki K.-i., Suzuki T. L., Yamamoto M., 2016, *ApJ*, 826, L28
- Hayashi M. et al., 2020, *PASJ*
- Hayashino T. et al., 2004, *AJ*, 128, 2073
- Hicks W., Wells A., Norman M. L., Wise J. H., Smith B. D., O’Shea B. W., 2020, *arXiv e-prints*, [arXiv:2009.05499](https://arxiv.org/abs/2009.05499)
- Iliev I. T., Mellema G., Shapiro P. R., Pen U.-L., Mao Y., Koda J., Ahn K., 2012, *MNRAS*, 423, 2222
- Inayoshi K., Haiman Z., Ostriker J. P., 2016, *MNRAS*, 459, 3738
- Inoue A. K. et al., 2016, *Science*, 352, 1559
- Ishigaki M., Ouchi M., Harikane Y., 2016, *ApJ*, 822, 5
- Iye M. et al., 2006, *Nature*, 443, 186
- Jeon M., Pawlik A. H., Bromm V., Milosavljević M., 2014, *MNRAS*, 440, 3778
- Johnson J. L., Dalla V. C., Khochfar S., 2013, *MNRAS*, 428, 1857
- Kennicutt Robert C. J., 1998, *ApJ*, 498, 541
- Khusanova Y. et al., 2020, *arXiv e-prints*, [arXiv:2007.08384](https://arxiv.org/abs/2007.08384)
- Kikuta S. et al., 2019, *PASJ*, 71, L2
- Kim C.-G., Ostriker E. C., 2015, *ApJ*, 802, 99
- Kistler M. D., Yüksel H., Beacom J. F., Hopkins A. M., Wyithe J. S. B., 2009, *ApJ*, 705, L104
- Komatsu E. et al., 2011, *ApJS*, 192, 18
- Kormendy J., Ho L. C., 2013, *ARA&A*, 51, 511
- Kubo M. et al., 2019, *ApJ*, 887, 214
- Lacaille K. M. et al., 2019, *MNRAS*, 488, 1790
- Latif M. A., Khochfar S., Whalen D., 2020, *ApJ*, 892, L4
- Lee K.-S. et al., 2012, *ApJ*, 752, 66
- Li Y., Gu M. F., Yajima H., Zhu Q., Maji M., 2020, *MNRAS*, 494, 1919
- Li Y., Hopkins P. F., Hernquist L., Finkbeiner D. P., Cox T. J., Springel V., Jiang L., Fan X., Yoshida N., 2008, *ApJ*, 678, 41
- Lim S., Scott D., Babul A., Barnes D., Kay S., McCarthy I., Rennehan D., Vogelsberger M., 2020, *arXiv e-prints*, [arXiv:2010.02259](https://arxiv.org/abs/2010.02259)
- Loiacono F. et al., 2020, *arXiv e-prints*, [arXiv:2006.04837](https://arxiv.org/abs/2006.04837)
- Luo Y., Shlosman I., Nagamine K., Fang T., 2020, *MNRAS*, 492, 4917
- Ma X., Quataert E., Wetzel A., Hopkins P. F., Faucher-Giguère C.-A., Kereš D., 2020, *MNRAS*, 498, 2001
- Madau P., Dickinson M., 2014, *ARA&A*, 52, 415
- Maiolino R. et al., 2008, *A&A*, 488, 463
- Mannucci F. et al., 2009, *MNRAS*, 398, 1915
- Marchesini D. et al., 2010, *ApJ*, 725, 1277
- Marconi A., Hunt L. K., 2003, *ApJ*, 589, L21
- Marrone D. P. et al., 2018, *Nature*, 553, 51
- Matsuda Y. et al., 2004, *AJ*, 128, 569
- Matsuda Y. et al., 2012, *MNRAS*, 425, 878
- Mawatari K. et al., 2020, *ApJ*, 889, 137
- Miller T. B. et al., 2018, *Nature*, 556, 469
- Mitsuhashi I. e. a., 2020, *submitted to MNRAS*
- Mo H. J., White S. D. M., 2002, *MNRAS*, 336, 112
- Mortlock A., Conselice C. J., Bluck A. F. L., Bauer A. E., Grützbauch R., Buitrago F., Ownsworth J., 2011, *MNRAS*, 413, 2845
- Murray N., Chiang J., Grossman S. A., Voit G. M., 1995, *ApJ*, 451, 498
- Murray N., Quataert E., Thompson T. A., 2005, *ApJ*, 618, 569
- Nagamine K., Choi J., Yajima H., 2010, *ApJ*, 725, L219
- Nelson D. et al., 2018, *MNRAS*, 475, 624
- Netzer H., 1987, *MNRAS*, 225, 55
- Nomura M., Ohsuga K., Done C., 2020, *MNRAS*, 494, 3616
- Oesch P. A. et al., 2016, *ApJ*, 819, 129
- Oesch P. A. et al., 2015, *ApJ*, 804, L30
- Omukai K., Tsuribe T., Schneider R., Ferrara A., 2005, *ApJ*, 626, 627
- Ono Y. et al., 2018, *PASJ*, 70, S10
- Onodera M. et al., 2016, *ApJ*, 822, 42
- Oteo I. et al., 2018, *ApJ*, 856, 72
- Oteo I., Zwaan M. A., Ivison R. J., Smail I., Biggs A. D., 2017, *ApJ*, 837, 182
- Ouchi M. et al., 2018, *PASJ*, 70, S13
- Overzier R. A., 2016, *A&A Rev.*, 24, 14
- Paardekooper J.-P., Khochfar S., Dalla Vecchia C., 2013, *MNRAS*, 429, L94
- , 2015, *MNRAS*, 451, 2544
- Pallottini A., Ferrara A., Gallerani S., Salvadori S., D’Odorico V., 2014, *MNRAS*, 440, 2498
- Park K., Ricotti M., 2011, *ApJ*, 739, 2

- Pearson W. J. et al., 2018, *A&A*, 615, A146
- Phipps F., Khochfar S., Varri A. L., Dalla Vecchia C., 2020, *A&A*, 641, A132
- Pillepich A. et al., 2018a, *MNRAS*, 475, 648
- Pillepich A. et al., 2018b, *MNRAS*, 473, 4077
- Planck Collaboration, 2016, *A&A*, 594, A13
- Planck Collaboration, 2020, *A&A*, 641, A6
- Proga D., Kallman T. R., 2004, *ApJ*, 616, 688
- Proga D., Stone J. M., Kallman T. R., 2000, *ApJ*, 543, 686
- Riechers D. A. et al., 2013, *Nature*, 496, 329
- Rosas-Guevara Y., Bower R. G., Schaye J., McAlpine S., Dalla Vecchia C., Frenk C. S., Schaller M., Theuns T., 2016, *MNRAS*, 462, 190
- Rosas-Guevara Y. M. et al., 2015, *MNRAS*, 454, 1038
- Schaye J. et al., 2015, *MNRAS*, 446, 521
- Schaye J., Dalla Vecchia C., 2008, *MNRAS*, 383, 1210
- Schaye J. et al., 2010, *MNRAS*, 402, 1536
- Shapley A. E., 2011, *ARA&A*, 49, 525
- Shimakawa R. et al., 2018, *MNRAS*, 473, 1977
- Shimizu I., Inoue A. K., Okamoto T., Yoshida N., 2014, *MNRAS*, 440, 731
- Shlosman I., Frank J., Begelman M. C., 1989, *Nature*, 338, 45
- Shlosman I., Noguchi M., 1993, *ApJ*, 414, 474
- Sijacki D., Vogelsberger M., Genel S., Springel V., Torrey P., Snyder G. F., Nelson D., Hernquist L., 2015, *MNRAS*, 452, 575
- Simpson J. M. et al., 2015, *ApJ*, 807, 128
- Song M. et al., 2016, *ApJ*, 825, 5
- Sparre M. et al., 2015, *MNRAS*, 447, 3548
- Springel V., 2005, *MNRAS*, 364, 1105
- , 2010, *MNRAS*, 401, 791
- Springel V., Frenk C. S., White S. D. M., 2006, *Nature*, 440, 1137
- Steidel C. C., Adelberger K. L., Shapley A. E., Pettini M., Dickinson M., Giavalisco M., 2000, *ApJ*, 532, 170
- Sugimura K., Hosokawa T., Yajima H., Omukai K., 2017, *MNRAS*, 469, 62
- Tacchella S. et al., 2015, *Science*, 348, 314
- Tadaki K. et al., 2018, *Nature*, 560, 613
- Tamura Y. et al., 2009, *Nature*, 459, 61
- Tanaka M. et al., 2019, *ApJ*, 885, L34
- Teyssier R., 2002, *A&A*, 385, 337
- Thornton K., Gaudlitz M., Janka H.-T., Steinmetz M., 1998, *ApJ*, 500, 95
- Toshikawa J. et al., 2018, *PASJ*, 70, S12
- Trebitsch M., Blaizot J., Rosdahl J., Devriendt J., Slyz A., 2017, *MNRAS*, 470, 224
- Trebitsch M. et al., 2020, arXiv e-prints, arXiv:2002.04045
- Tremmel M., Karcher M., Governato F., Volonteri M., Quinn T. R., Pontzen A., Anderson L., Bellovary J., 2017, *MNRAS*, 470, 1121
- Troncoso P. et al., 2014, *A&A*, 563, A58
- Umehata H. et al., 2019, *Science*, 366, 97
- Umehata H. et al., 2018, *PASJ*, 70, 65
- Umehata H. et al., 2020, *A&A*, 640, L8
- Umehata H. et al., 2015, *ApJ*, 815, L8
- Vogelsberger M., Genel S., Springel V., Torrey P., Sijacki D., Xu D., Snyder G., Nelson D., Hernquist L., 2014, *MNRAS*, 444, 1518
- Wada K., 2012, *ApJ*, 758, 66
- Walter F. et al., 2018, *ApJ*, 869, L22
- Wang T. et al., 2019, *Nature*, 572, 211
- Watarai K.-y., Fukue J., Takeuchi M., Mineshige S., 2000, *PASJ*, 52, 133
- Wise J. H., Demchenko V. G., Halicek M. T., Norman M. L., Turk M. J., Abel T., Smith B. D., 2014, *MNRAS*, 442, 2560
- Wise J. H., Turk M. J., Norman M. L., Abel T., 2012, *ApJ*, 745, 50
- Wolcott-Green J., Haiman Z., Bryan G. L., 2011, *MNRAS*, 418, 838
- , 2017, *MNRAS*, 469, 3329
- Yajima H., Choi J.-H., Nagamine K., 2011, *MNRAS*, 412, 411
- , 2012a, *MNRAS*, 427, 2889
- Yajima H., Li Y., Zhu Q., 2013, *ApJ*, 773, 151
- Yajima H., Li Y., Zhu Q., Abel T., 2015a, *ApJ*, 801, 52
- Yajima H., Li Y., Zhu Q., Abel T., Gronwall C., Ciardullo R., 2012b, *ApJ*, 754, 118
- , 2014, *MNRAS*, 440, 776
- Yajima H., Nagamine K., Zhu Q., Khochfar S., Dalla Vecchia C., 2017a, *ApJ*, 846, 30
- Yajima H., Ricotti M., Park K., Sugimura K., 2017b, *ApJ*, 846, 3
- Yajima H., Shlosman I., Romano-Díaz E., Nagamine K., 2015b, *MNRAS*, 451, 418
- Yajima H., Sugimura K., Hasegawa K., 2018, *MNRAS*, 477, 5406
- Yajima H., Umemura M., Mori M., 2012c, *MNRAS*, 420, 3381